ANNALS OF GEOPHYSICS, 67, 4, S427, 2024; doi:10.4401/ag-9142
OPEN ACCESS

Use of tsunami observations for resolving coseismic slip of recent and historic large submarine earthquakes

Thorne Lay*[,1], Fabrizio Romano[2], Stefano Lorito[2]

(1) University of California Santa Cruz, Earth and Planetary Sciences Department, Santa Cruz, CA, USA
(2) Istituto Nazionale di Geofisica e Vulcanologia, Roma, Italy

Article history: received August 20, 2024; accepted September 17, 2024

Abstract

Tsunamis generated by seafloor displacements accompanying large submarine earthquakes provide sensitivity to absolute slip position and distribution for offshore faulting analogous to that of geodetic observations for landward faulting. Tsunami recordings at deep-water and near-shore ocean bottom pressure sensors and tide gauges, along with runup and inundation measurements, can now be reliably modeled using detailed bathymetric structures and robust numerical codes. As a result, tsunami observations now play an important role in quantifying coseismic slip distributions for large submarine earthquakes in subduction zones and other tectonic environments. Applications of joint modeling or inversion of seismic, geodetic and tsunami observations for recent major earthquakes are described, highlighting the specific contributions of the tsunami observations to source model resolution. Tsunami observations provide unique information on the up-dip extent of earthquake coseismic slip on subduction zone megathrust faults and occurrence of near-trench slip, which are usually not well constrained by seismic and land-based geodetic signals. Tsunami signals also help to detect offshore slow slip that is not evident in seismic or land-based geodetic data and to balance geophysical constraints on ruptures that extend from on-shore to off-shore. Tsunami runup measurements and stratigraphic deposits further provide unique constraints on large earthquake ruptures that occurred prior to modern geophysical instrumentation.

Keywords: Tsunami Modeling; Earthquake Slip Models; Tsunamigenic Earthquakes; Submarine Faulting; Tsunami Runup

1. Introduction

The Earth has experienced about one great ($M_W \geq 8.0$) shallow depth (≤ 70 km) earthquake each year during this century, all of which have been tsunamigenic to varying extent. Tsunamis, which are oceanic long-period gravity waves produced by these events, have sometimes been devastating, notably for the 2004 Sumatra-Andaman M_W 9.2 (Lay et al., 2005; Shearer and Bürgmann, 2010) and 2011 Tohoku M_W 9.1 (Lay, 2018) earthquakes. The 2004 event, and the subsequent 2011 event, prompted the expanded deployment of continuously telemetered deep-water

ocean bottom pressure sensors to enhance Pacific-wide tsunami warning capabilities (e.g., Deep-ocean Assessment and Reporting of Tsunamis (DART) buoys and Japan's S-net cable system), and together with progressively higher-resolution sea floor bathymetry models and tsunami numerical modeling capabilities (e.g., Yamazaki et al., 2023) this transitioned tsunamis from primarily hazardous phenomena to valuable conveyors of information about their sources. Most sources of tsunamis involve slip on offshore faults that displace the seafloor and overlying ocean water, exciting oceanic gravity waves. There is a long history of earlier applications of tsunami observations to study faulting sources that primarily utilized tsunami arrival times and amplitudes at tide gauge recordings and runup/inundation measurements, calculation of which were limited by availability of only low-resolution bathymetry, especially in the shallow water environments around coastal regions, and limited hydrostatic tsunami modeling codes. The transition to quantitative analysis of earthquake finite-fault sources involving modeling and inversion of combined seismic, geodetic, and tsunami observations has been discussed in prior reviews by the authors (Lorito et al., 2016; Romano et al., 2020a). Here, we build on these earlier discussions of tsunamigenic events, focusing on events since 2018 along with some Hawaiian and Aleutians historical events, emphasizing the specific contributions of tsunami observations to improved source representations.

Inversions for coseismic slip distributions of large subduction zone earthquakes are now commonly performed, using rapidly available seismic and geodetic data sets (e.g., Crowell and Melgar, 2020; Liu et al., 2020; Xiao et al., 2021; Elliot et al., 2022; Goldberg et al., 2022; Liu et al., 2022; Zhao et al., 2022). The resulting slip models guide interpretations of the seismic cycle, earthquake hazard, afterslip and aftershock occurrence, and frictional behavior of the megathrust fault, so their resolution is important. While teleseismic data usually provide good azimuthal coverage for steep take-off angles, regional seismic and geodetic data (GNSS and InSAR) typically provide only landward coverage. As a result, the seaward distribution of inverted slip for plate boundary thrust events and outer rise extensional events is usually not well resolved in separate or joint inversions of seismic and land-based geodetic data, and the same holds for inferences of interseismic slip deficit from land-based geodetic data (e.g., Herman et al., 2018; Williamson and Newman, 2018; Lindsey et al., 2021; Xiao et al., 2021; Zhao et al., 2022). Seafloor geodesy can contribute to constraining shallow coseismic rupture and near-trench slip deficit (e.g., Iinuma et al., 2012, DeSanto et al., 2023, Brooks et al., 2023), but, as yet, such instrumentation remains sparsely deployed and is often collected in campaign mode providing limited time resolution. However, incorporation of rapidly available tsunami data in finite-source inversions can improve resolution of offshore slip. Shallow slip amplification in megathrust earthquakes may be caused by dynamic and anelastic processes enhancing the tsunami generation efficiency (Murphy et al., 2016; Lotto et al., 2017; Murphy et al., 2018; Ma, 2023), and this shallow slip may remain partly undetected except by tsunami observations.

The great 2010 Maule, Chile M_W 8.8 and 2011 Tohoku, Japan M_W 9.1 earthquakes were well-recorded by seafloor pressure sensors regionally and globally, allowing finite-fault inversions to include high quality tsunami waveform data (in addition to tide gauge observations), demonstrating the value-added for resolving offshore slip. Figure 1 shows a checkerboard test for a complex specified slip distribution in the Maule region separately inverted using the corresponding synthetic signals from high-rate GPS (Hr-GPS), teleseismic, coseismic static offsets from InSAR and campaign GPS (cGPS), and four offshore DART sensors, and for a joint inversion (Yue et al., 2014a). The recovery of the input slip distribution varies for each data set (Fig. 1b-e) due to their distribution and intrinsic resolution, but it is evident that the geodetic data sets provide stable recovery of slip below land while the tsunami data stably recovers slip below water. Suitable weighting of the various data in a joint inversion achieves good recovery of the full model (Fig. 1f) due to the complementary sensitivity. Similar results for the 2011 Tohoku event were presented in Yokota et al. (2011), Romano et al. (2012) and discussed in Lorito et al. (2016). While very long-period waves, the low speed of tsunami contributes to their good resolution of offshore slip.

The added spatial resolution of submarine fault slip provided by tsunami waveform observations has played an important role in constraining finite-fault models for many earthquakes since 2004. Lorito et al. (2016) review the tsunami observations and source imaging applications to important very large shallow events up to 2013: 2004 Sumatra-Andaman M_W 9.2; 2005 Nias M_W 8.6; 2006 Java M_W 7.8; 2006-2007 Kuril interplate/intraplate doublet M_W 8.3/8.1; 2007 Bengkulu M_W 8.4; 2007 Peru M_W 8.0; 2007 Solomon Islands M_W 8.1; 2009 Samoa intraplate/interplate doublet M_W 8.1/8.0; 2010 Maule M_W 8.8; 2010 Mentawai M_W 7.8; 2011 Tohoku M_W 9.1; 2012 Haida Gwaii M_W 7.8; 2012 Indian Plate M_W 8.7 intraplate; and 2013 Santa Cruz Islands M_W 8.0. Romano et al. (2020a) extend the review and include the 2014 Iquique M_W 8.1; 2015 Illapel M_W 8.4; 2016 Kaikoura M_W 7.8 strike-slip; 2017 Chiapas, Mexico M_W 8.2 intraslab; and 2018 Palu M_W 7.5 strike-slip earthquakes. Here we discuss more recent studies in which analysis of tsunami observations with and without other geophysical data sets has contributed

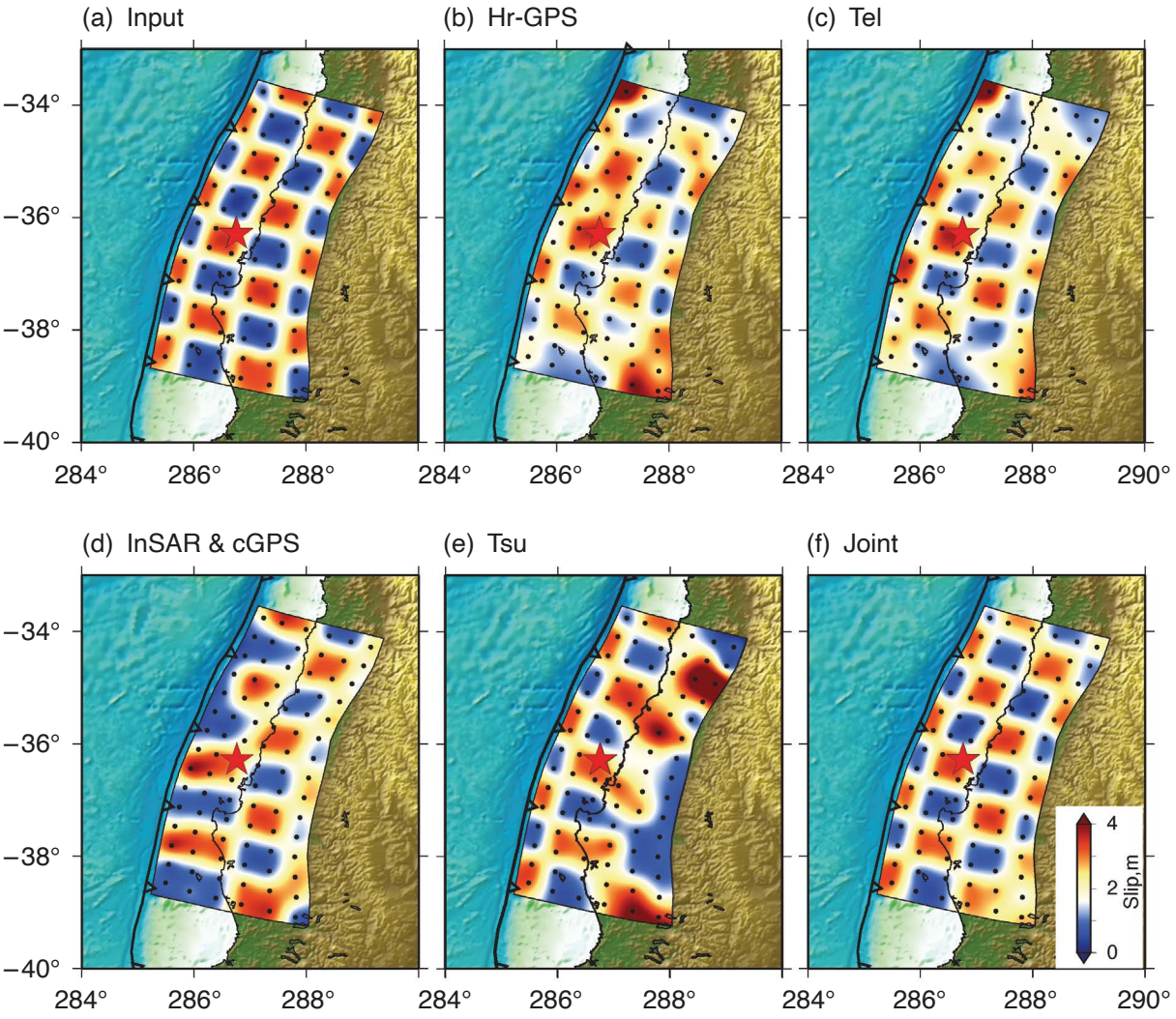

Figure 1. Tests of resolution for finite-fault inversions of distinct data sets computed for (a) a specified input checkerboard slip distribution for the 2010 Maule, Chile M_W 8.8 earthquake. Inversions using corresponding synthetics for the actual distributions of (b) displacement time series from 7 Hr-GPS stations, (c) teleseismic P and SH wave ground displacements, (d) static displacements from InSAR and 82 campaign cGPS stations, (e) tsunami recordings at 4 offshore DART stations, and (f) joint inversion of all data sets. Note the complementary on-shore/off-shore patterns of the InSAR and cGPS and tsunami images, which combine to give overall good joint recovery of the input model when appropriate relative data weights are used. From Yue et al. (2014a).

to resolving faulting source processes of recent megathrust events with $M_W \geq 7.7$, a smaller tsunami earthquake, several intraplate ruptures, volcanic décollement ruptures, and several historic megathrust events. A broad range of tsunami modeling contributions to source imaging is demonstrated by this recent work. Tsunami observations and modeling have also played critical roles in quantifying recent volcanic landslide (Anak Krakatau, 2020) and eruption (2022 Hunga-Tonga) processes, but the focus here is on earthquake-generated tsunami.

2. Tsunamigenic Events

While the annual rate of great shallow earthquakes in the last decade has slowed relative to the unusually high rate experienced from 2004 to 2014 (Lay, 2015), tsunami recordings have continued to play an important role in constraining the finite-fault source models of all recent shallow submarine events with $M_W \geq 7.7$ other than for the 28 January 2020 Cayman Islands M_W 7.7 strike-slip event. Improvements in tsunami runup and inundation modeling have also allowed better resolution of important historic events that either have limited, or no seismic and geodetic

observations. Most tsunami calculations shown in this paper use the well-vetted non-hydrostatic code NEOWAVE (Yamazaki et al., 2023), which can model non-hydrostatic aspects of tsunami generation and dispersive propagation, for which the importance depends on the specific seismic event size, duration, and context (Abrahams et al., 2023; Abbate et al., 2024; Scala et al., 2024). While simpler shallow-water-based codes can be sufficient for hazard and early warning applications, these properties of NEOWAVE avoid inaccuracies in tsunami modelling that are mapped onto the source model, potentially affecting the quality of the results of source inversion studies. However, NEOWAVE does not consider water compressibility, Earth's elasticity, and tsunami-induced gravity changes (Watada, 2013; Watada et al., 2014), which can be accounted for with appropriate corrections of the Green's functions used in the inversions (e.g., Romano et al., 2020b; Heidarzadeh and Gusman, 2021). Recent studies reaffirm and extend the value of tsunami modeling for constraining diverse source processes discussed in prior reviews (Lorito et al., 2016; Romano et al., 2020a).

2.1 Recent Megathrust Events

Large subduction zone plate boundary (megathrust) earthquakes involve underthrusting motions that tend to produce strong seaward up-lift and weaker landward down-drop of the seafloor of the upper plate that generates tsunamis. Horizontal motions of the dipping bathymetry augment the up-lift, and this must be included in modeling tsunami excitation (e.g., Tanioka and Satake, 1996). The value of incorporating tsunami observations into the source quantification is reaffirmed by recent studies of large megathrust events.

2.1.1 28 July 2021 Chignik, Alaska Peninsula (M_W 8.2)

One of the largest megathrust ruptures of the past six years was the 29 July 2021 M_W 8.2 Chignik, Alaska Peninsula event. This event (Fig. 2) ruptured within the Semidi segment of the Pacific-North American plate boundary, offshore of the Alaska Peninsula. This portion of the megathrust last experienced a great earthquake rupture in 1938 (M_W 8.2), and the two events have significant rupture overlap. Some geodetic estimates of slip deficit had suggested strong locking extending to the trench (Li and Freymueller, 2018; Droof and Freymueller, 2021), raising the possibility of shallow, strongly tsunamigenic rupture. One has to be cautious about such an inference given the relatively poor resolution at shallow depths offered by geodetic inversions from inland instruments (see Fig. 1, or, for example, Romano et al., 2010). The 2021 earthquake, like the 1938 event, was not strongly tsunamigenic, and large coseismic slip was concentrated on the megathrust below a very shallow (100-200 m deep) continental shelf (Fig. 2b). Ruptures confined to the megathrust below a flat continental shelf occur seldomly (e.g., Ye et al., 2016; Mulia et al., 2022a, b), and the tsunami generated in the shallow water layer tends to be very long-period. As tsunami wave energy leaks out into deeper water overlying the continental slope and trench, strong de-shoaling occurs, resulting in relatively low far-field tsunami amplitudes, and this can account for the weak 1938 and 2021 observations.

Seismic and on-land geodetic data were rapidly inverted for the 2021 event (Liu et al., 2022; Elliott et al., 2022; Zhao et al., 2022), resulting in slip models extending from 9 to 46 km depth. Tsunami data were jointly analyzed soon after (Ye et al., 2022; Mulia et al., 2022b; Liu et al., 2023a), demonstrating that slip exceeding ~1 m did not occur on the megathrust at depths less than 22 km. The analyses with tsunami observations provide improved resolution of the up-dip limit of significant slip relative to the seismic and on-land geodetic observations by matching both absolute time and amplitude of the first tsunami arrivals at seaward ocean bottom pressure sensors of the DART stations, the positions of some of which are shown in Fig. 3. The available bathymetry for the deeper water regions is sufficiently well resolved to provide accurate arrival time calculations for the long-period de-shoaling tsunami waves, and if any significant displacement occurred along the continental slope, relatively strong short-period tsunami energy would be excited (e.g., Mulia et al., 2022b; Bai et al., 2022), which provides a strong constraint on the up-dip extent of coseismic slip.

As a demonstration of the acute sensitivity of the tsunami excitation to up-dip limit of slip for the 2021 event, comparisons of slip distribution and seafloor deformation for two slip models (Liu et al., 2022; Liu et al., 2023a) are shown in Fig. 4. The starting model (Fig. 4a), based on joint inversion of extensive teleseismic, regional seismic, and on-land geodetic observations (Liu et al., 2022) has coseismic slip concentrated at depths greater than 20 km (as do all of the finite-source models), but with modest slip of 1-2 m extending up-dip to below the shelf break

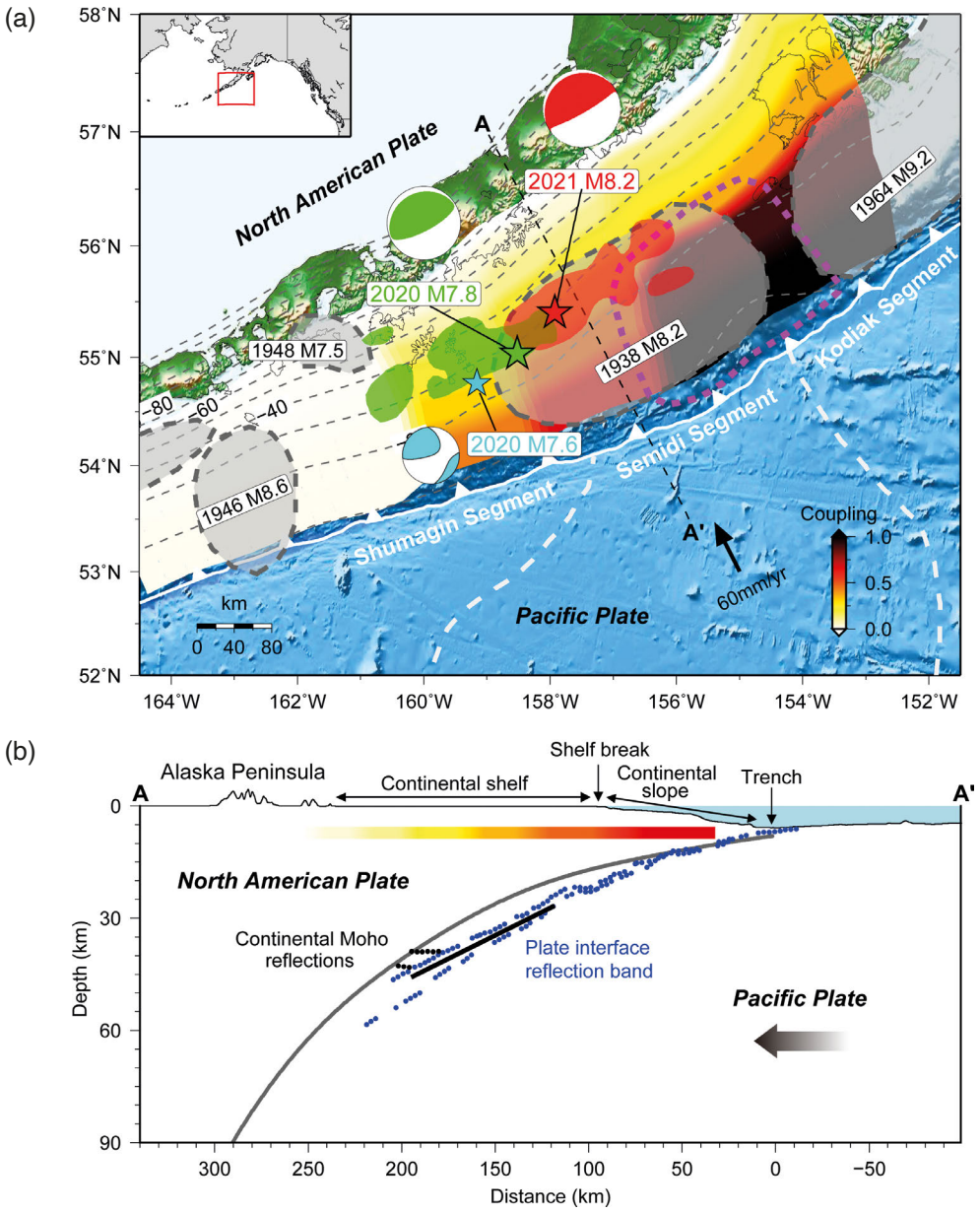

Figure 2. Regional tectonic setting of the Alaska-Aleutian subduction zone and cross-section through the Semidi segment. (a) The gray shaded patches with dashed lines indicate the rupture regions of 1938, 1946, 1948, and 1964 events. The coseismic rupture areas of the 2020 M_W 7.8 Simeonof event (Bai et al., 2022) and 2021 M_W 8.2 Chignik event (Liu et al., 2023a) are indicated with green-filled and red-filled patches, respectively. The thick magenta dashed line outlines the 1938 tsunami source model determined by Freymueller et al. (2021). The stars and focal mechanisms indicate the epicenters and GCMT solutions of the 22 July 2020 Shumagin mainshock (green), the 19 October 2020 Shumagin intraplate aftershock (cyan), and the 29 July 2021 Semidi mainshock (red), respectively. Depths to the plate interface from Slab2 are shown by gray dashed lines with an interval of 10 km (Hayes et al., 2018). The plate coupling distribution is from Li and Freymueller, (2018). The white barbed line shows the plate boundary trench between the Pacific plate and the North American plate, and the black arrow shows the relative motion between the Pacific plate and the North American plate (DeMets et al., 1994). White dashed lines outline the margins of the Zodiak Fan. The inset shows the general location of the study area. (b) Cross-section indicating the Liu et al. (2023a) fault model for the 2021 Chignik event and the geometry of the plate interface, highlighting the broad flat continental shelf overlying the rupture zone, the shelf break, and the continental slope. Two blue dotted lines represent the thickness range of seismic reflection packages associated with the boundary zone of the plate interface (Kuehn, 2019). The black dotted lines show the extent of continental Moho. The thick gray curve is the slab interface profile from the Slab2 model along profile AA′ in (a), which is about 6 km too shallow. Modified from Liu et al. (2023a).

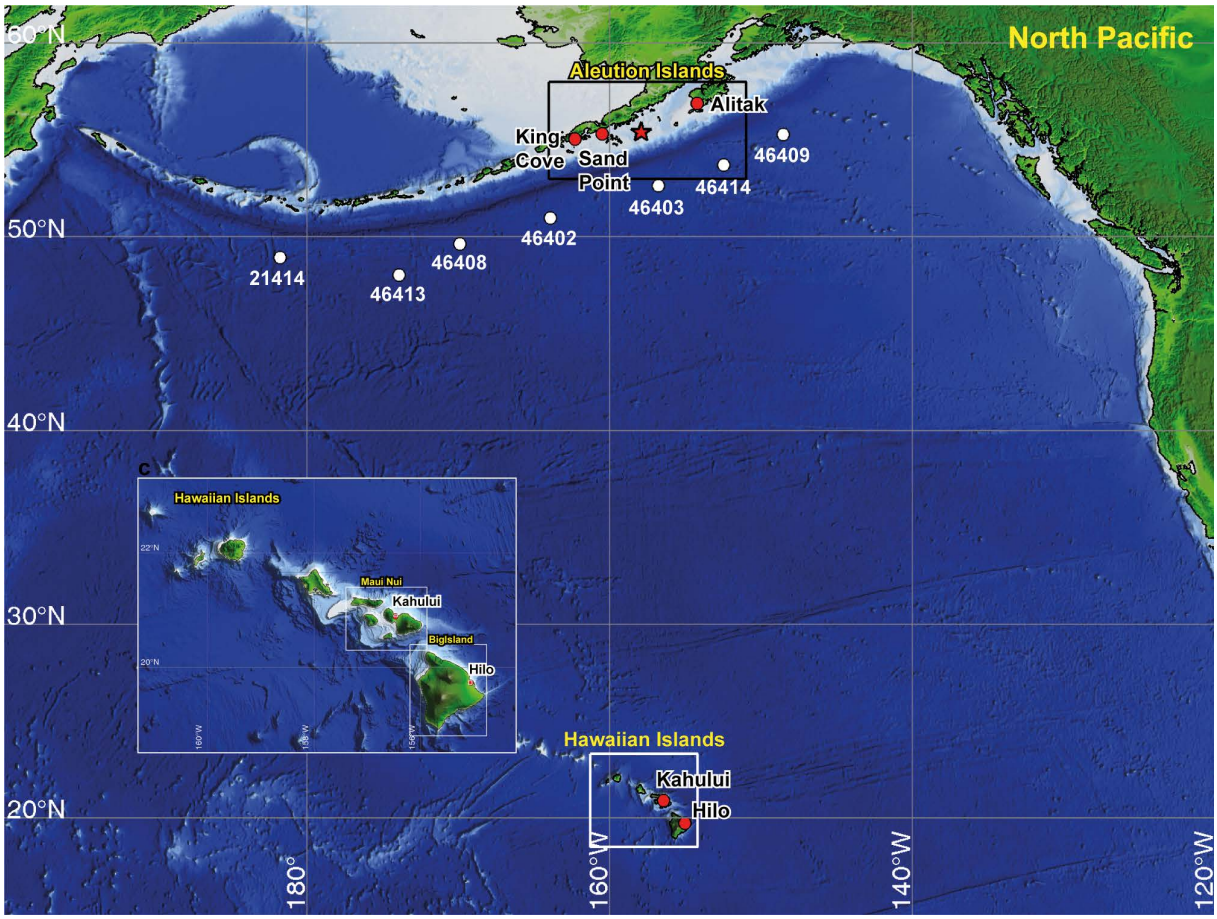

Figure 3. Computational bathymetry and location maps of tide gauge and DART stations. Level-1 grid with outlines of level-2 grids, DART locations (white circles), and Sand Point, King Cove, Alitak, Kahului, and Hilo tide gauges (red circles). Inset: Level-2 grid for the Hawaiian Islands with outlines of level-3 and 4 grids. Modified from Liu et al. (2023a).

(Fig. 2), which produces deformation of up to 0.5 m on the continental slope. This will result in early first tsunami arrivals (tsunami waves in the deepening water along the continental slope travel faster than tsunami waves under the shallow continental shelf), and large shorter period tsunami energy excited by seafloor displacement under deeper water. As seen in Fig. 5 (left column), the calculated first tsunami pulses arrive too early and are too short-period and too large at DART stations, for this otherwise acceptable starting model; the same behaviour is found for other inversions of only seismic and geodetic data. The too strong excitation of seaward short-period tsunami waves energy is also clearly evident at the Hawaiian tide gauges. By iteratively constraining the up-dip boundary of the finite-source model to greater depth, reinverting the seismic and geodetic data (achieving the same overall fits), and modeling the tsunami signals, Liu et al. (2023a) obtained greatly improved fits to the DART recordings of tsunami first arrival time and amplitude and full waveform spectra (Fig. 5a, right column) for a model with slip constrained to depths of 26 to 42 km. While errors in bathymetry can lead to arrival time misalignments and strategies to remove any bias this may cause in the modeling have been proposed (e.g., Romano et al., 2016, 2020b), any alignment errors are expected to be small for the short paths to the DART stations while 2 minute shifts have been applied to the distant Hawaiian tide gauge signals. The long sequence of coastal reflections that follows the first arrival is also better modeled by the updated model, as are the tide gauge signals at both regional (Fig. 5b) and far-field distances (Fig. 5c).

Given that the updated model provides good matches to teleseismic, regional seismic, on-land GNSS, and DART and tide gauge recordings, the slip distribution (Fig. 2a and 4b) is a viable model for the rupture. A surprising aspect of the slip model is that it locates within a distributed reflectivity zone (from marine seismic imaging) thickening from 2 to 5 km with depth (Fig. 2b), whereas the shallower megathrust that did not host significant coseismic slip has a much narrower, well-defined interface. This sustains the question of whether the shallower megathrust in this

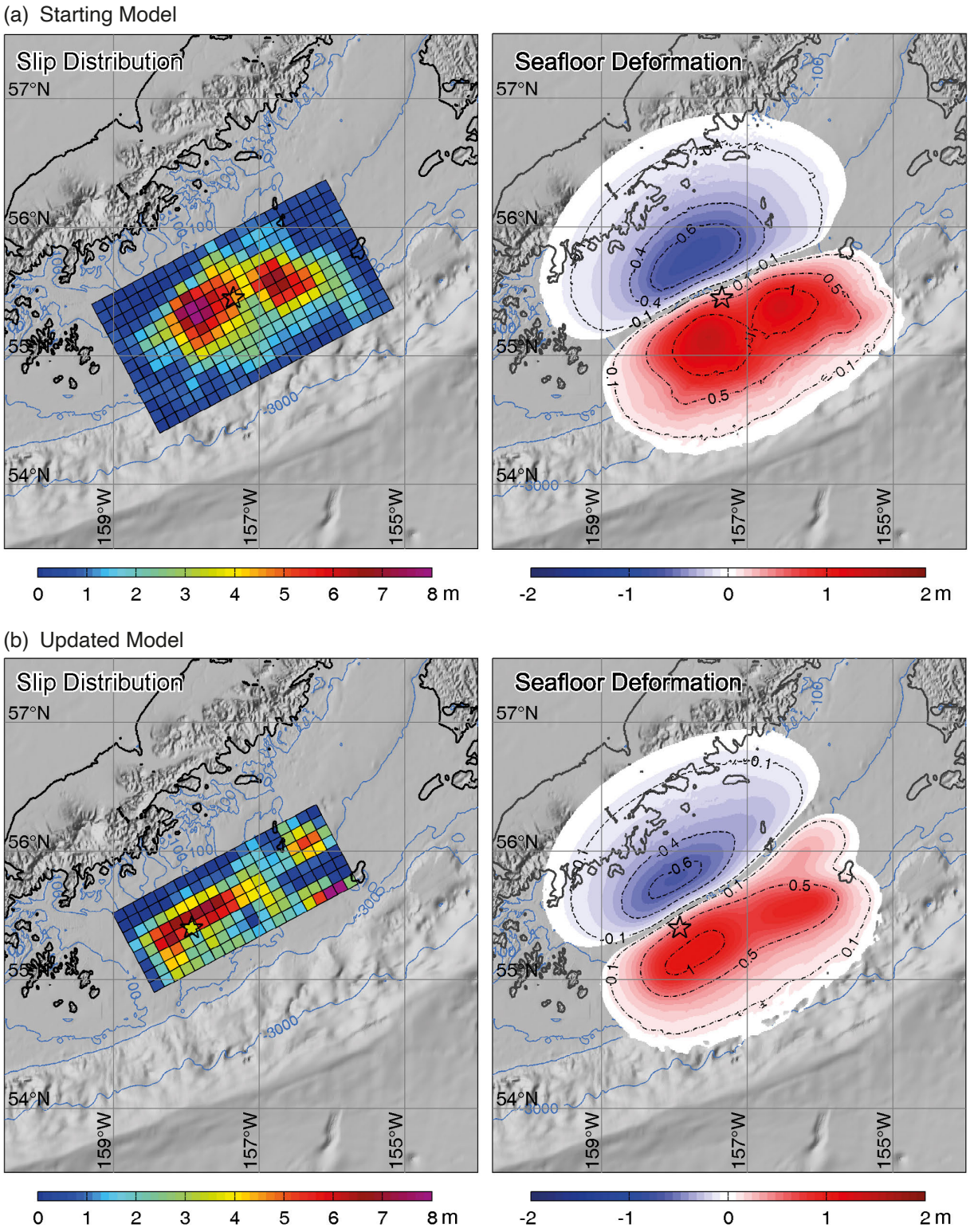

Figure 4. Starting and final slip models for the 2021 Chignik, Alaska Peninsula earthquake. (a) Slip distribution (left) and vertical seafloor deformation (right) for the starting model from Liu et al. (2022). The star indicates the hypocenter from an initial USGS-NEIC location (55.325°N, 157.841°W, 32.2 km deep). (b) Slip distribution (left) and vertical sea floor deformation (right) for the final model, which fits all data well. Water depth contours of 100 m, 300 m, and 3000 m are shown by light blue dashed lines. The star indicates the USGS-NEIC hypocenter (55.364°N, 157.888°W, 35 km deep). From Liu et al. (2023a).

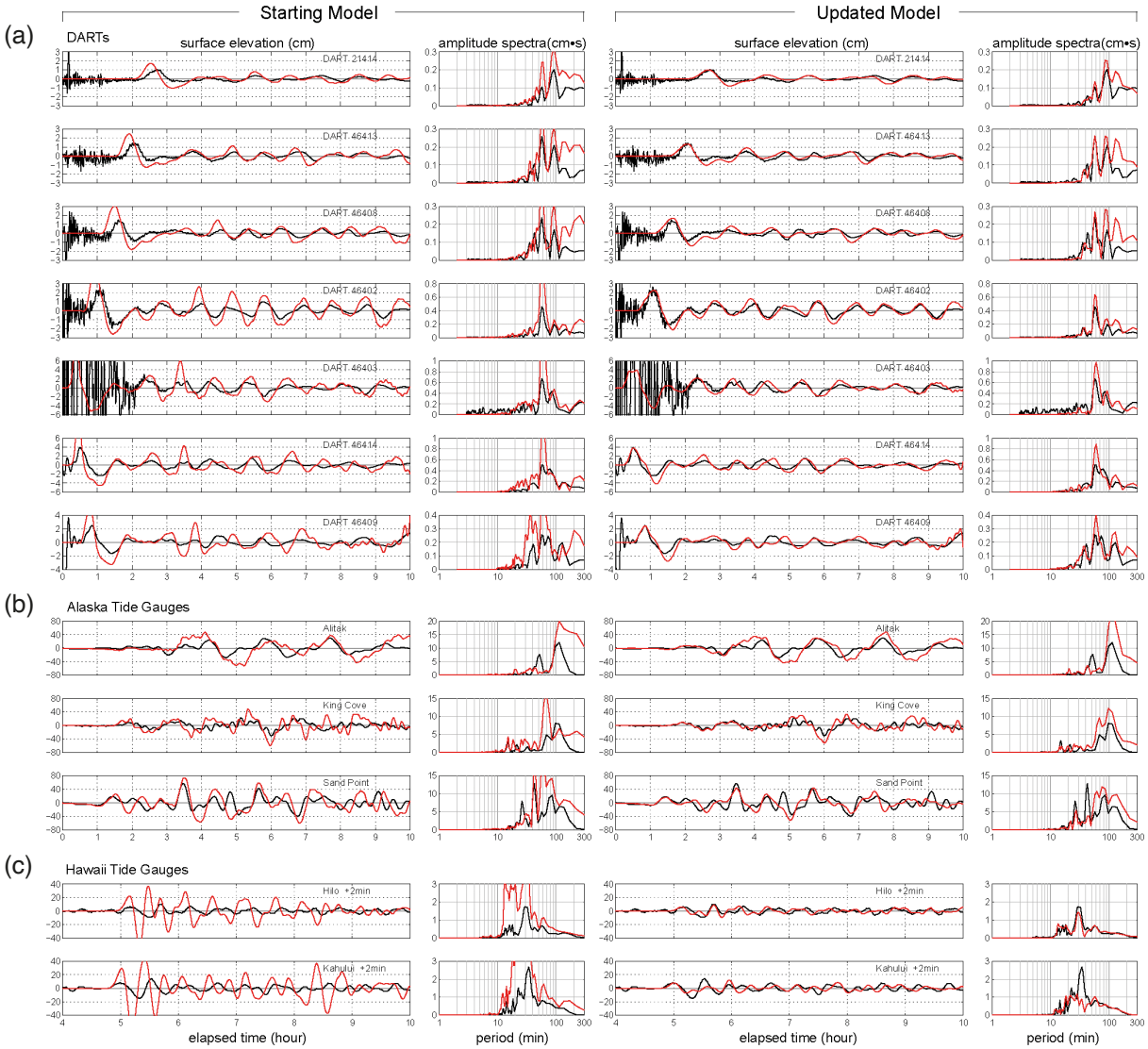

Figure 5. Tsunami observations and model predictions at (a) regional DART stations, and (b) Alaska and (c) Hawaiian tide gauges for the two finite-fault slip models in Fig. 4. Comparisons on the left are for the starting seismic and geodetic model in Fig. 4a from Liu et al. (2022), while those on the right are for the updated slip model in Fig. 4b, which has been adjusted to fit the tsunami data simultaneously with the seismic and geodetic data. From Liu et al. (2023a).

region can accumulate strain and host a shallow tsunami earthquake under the continental slope or is experiencing aseismic deformation. A seafloor GNSS_a sensor located up-dip of the 2021 hypocenter indicates that large afterslip occurred at shallow depth (Brooks et al., 2023), and a concentration of moderate aftershock activity up-dip of the coseismic slip zone (Liu et al., 2023a), suggests that the up-dip region is at least not uniformly strongly-locked, if at all, so a very large tsunami earthquake appears unlikely, except perhaps as part of a very large earthquake (larger than in 1938 or 2021) that nucleates deeper for which shallow slip amplification is more likely to occur (Murphy et al., 2016, 2018; Scala et al., 2019, 2020).

2.1.2 12 August 2021 South Sandwich Islands (M_W ~8.25)

A great thrust earthquake with M_W ~8.25 struck the South Sandwich Islands megathrust on 12 August 2021. The rupture process was complex and lasted ~225-240 s, with a sequence of discrete ruptures at varying depths distributed along ~440 km of the strongly curved arc, where the southern Atlantic plate underthrusts the small Sandwich Plate at ~7 cm/yr (Fig. 6). The event generated far reaching tsunamis detected at tide gauges and DART stations in the north Atlantic, Pacific and Indian Oceans (e.g., Jia et al., 2022; Metz et al. 2022). Jia et al. (2022) analyzed seismic data for the event, producing a model with overall southward progression of 5 subevents with M_W 7.2, 7.2, 8.16, 7.6 and 7.7 combining for a total M_W 8.24. The largest subevent has an ~180 s long duration with 1 km/s rupture velocity at shallow depth (14 ± 5 km) over 180 km along the 4° dipping megathrust. This is essentially a slow earthquake bracketed along strike by smaller regular thrust subevents. The slow slip component is somewhat deeper than for most observed tsunami earthquakes, which tend to have rupture shallower than ~15 km, and combined with a lack of low rigidity sediments near the toe, this may have reduced the tsunami excitation. Metz et al. (2022) further explored the source with moment tensor, pseudo dynamic finite-fault inversion, and teleseismic back-projection applications, favouring a similar four-subfault model with slow slip along the shallow megathrust extending southward with changing strike (Fig. 6).

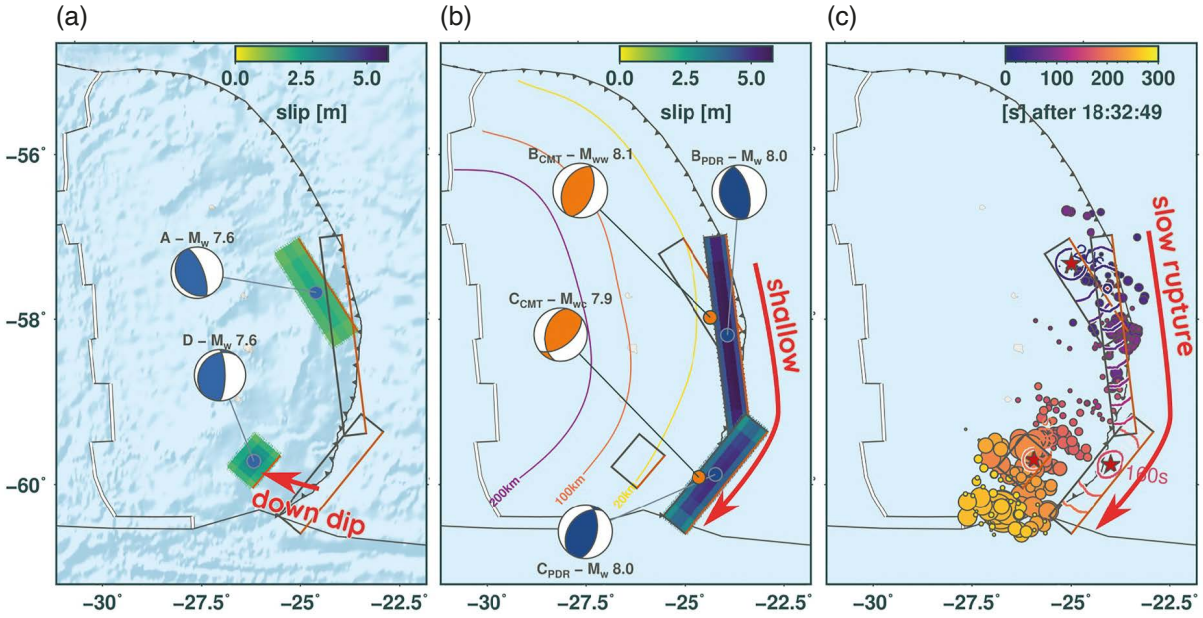

Figure 6. Results of the four-subfault analysis of the 2021 South Sandwich Islands rupture process by Metz et al. (2022). (a) Final static slip maps and associated centroid moment tensors retrieved from body wave inversions (0.01-0.05 Hz) for subevents A and D using the pseudo dynamic rupture (PDR). (b) The results for very low frequency CMT and PDR inversions of subevents B and C. Rectangular outlines in (a) and (b) show the location of the PDR solutions for subevents B, C or A, D, respectively (visualizes spatial relationships between the overlapping rupture planes). (c) The kinematics of the rupture. Contours indicated rupture propagation derived from PDR with respective subevent origins as red stars. Dots show high-frequency energy emitters (0.5-2 Hz, size scales with energy release) from back-projection. Modified from Metz et al. (2022).

Simplified tsunami modeling (Metz et al., 2022) for the M_W 8.2-8.25 slow slip component using instantaneous fault slip and offshore computation of the tsunami signals produced reasonable fits to first oscillation timing, shape and amplitude at five tide gauge recordings in the southern Atlantic and southern Indian ocean (Fig. 7b), using time-shift adjustments for the off shore-to-on shore propagation based on the Optimal Time Alignment (OTA) procedure of Romano et al. (2016). In this case, the tsunami modeling serves primarily as a validation of the complex shallow tsunamigenic slip of the model. Maximum wave amplitudes of up to > 1 m were computed for the strong east and west lobes of the tsunami radiation pattern (Fig. 7a).

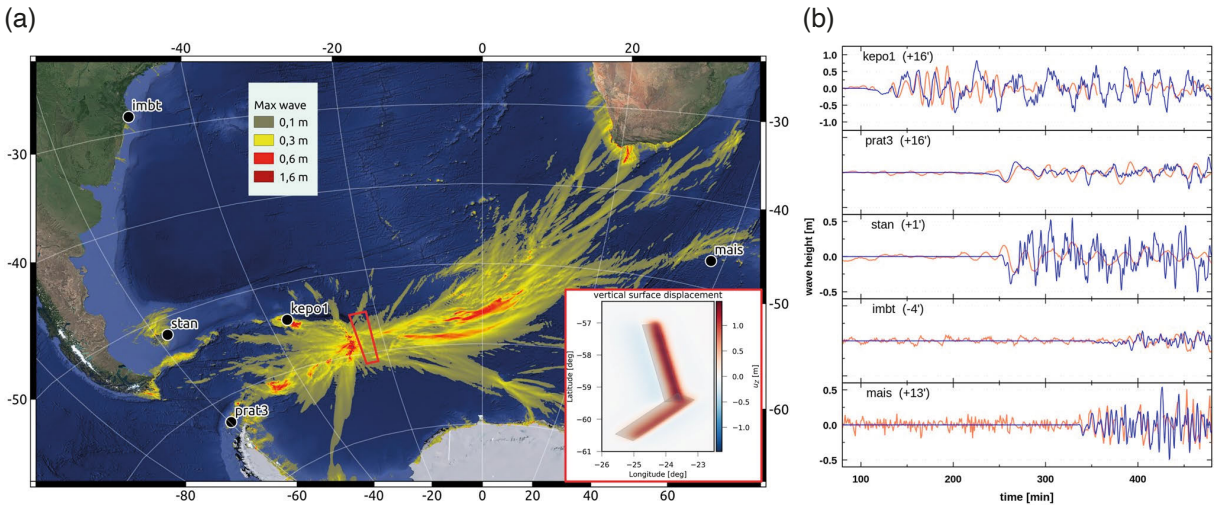

Figure 7. Forward tsunami modeling with initial conditions corresponding to the vertical seafloor displacement as predicted by the PDR model results for subevents B and C in Fig. 6b. Tsunami triggering is assumed as instantaneous vertical displacement of the seafloor at the joint centroid time of 18:34:46. (a) Maximum tsunami wave heights (values <0.1 m clipped). Also shown are positions of tide gauges. The insert indicates initial conditions for tsunami modeling located within the red box on the map. (b) Modeled (blue) versus observed (red) mareograms at the tide gauges sorted by distance to the epicenter. Values in brackets indicate additional time shifts in (min) applied for the optimal fit (see Romano et al., 2016). Note that all data except "kepo1" are plotted in the same scale. From Metz et al. (2022).

2.1.3 4 March 2021 Kermadec Islands (M_W 8.1)

The northern Kermadec Islands subduction zone near Raoul Island was struck by a thrusting sequence involving an M_W 7.4 foreshock followed 1 hr 47 min later by an M_W 8.1 mainshock. The latter event is the largest well-documented event to rupture on the Tonga-Kermadec megathrust. The mainshock generated a moderate tsunami that was well-recorded at New Zealand DART network stations and tide gauges in Tonga, Vanuatu, New Zealand, Hawai'i, Galapagos, the Austral Islands and in Crescent City, California, USA (Romano et al., 2021; Wang et al., 2022). Romano et al. (2021) inverted tsunami recordings from tide gauges and DART stations, finding northeastward rupture along 130 km with slip of up to 5 m concentrated from 20-30 km depth, and minor, weakly-constrained slip on the shallow megathrust. Wang et al. (2022) used tsunami signals from the foreshock as empirical Green's functions for the mainshock, helping to isolate the dominant energy in the 8-32 min range for the second tsunami, with spectral peaks at 25.6, 16.0 and 9.8 min.

Lythgoe et al. (2023) derived finite-fault models for the foreshock and mainshock by inversion of teleseismic body wave data, also finding northeastward rupture, with large slip confined between depths of 50-60 km for the foreshock and 20 and 50 km for the mainshock. Minor, poorly resolved slip is again present on the shallow megathrust for the mainshock rupture model. Ye et al. (2024) inverted teleseismic body wave data along with static offsets at the GNSS station Raul on Raoul Island (Fig. 8a) and validated the slip models by comparisons with the tsunami waveforms modeled by Romano et al. (2021), also finding that all major slip for the two events is on the plate interface from 20 to 55 km deep (Fig. 8b). For this island arc subduction zone, the upper plate crust is about 17 km thick, based on reflection imaging, which indicates that this great earthquake sequence ruptured on the mantle/slab contact. This is the first clearly documented case of such a rupture and has broad implications for seismic hazard in other island arc settings where it is commonly assumed that the maximum depth of likely ruptures is defined by the upper plate Moho. Comparisons of teleseismic waveforms with those for a sequence of prior large events in 1976 suggest that the mantle/slab contact also ruptured in the earlier sequence with some overlap of slip (Lythgoe et al., 2023; Ye et al., 2024), but the events are not precise repeaters. The tsunami observations for this event are primarily valuable in precluding significant coseismic slip from having occurred on the shallower megathrust. The crust/slab contact up-dip of the large slip zone in 2021 has had active moderate size background faulting and many moderate size aftershocks occurred just up-dip of the 2021 large-slip zone similar to the behaviour for the 2021 Chignik earthquake (Section 2.1.1), so the shallow interface does not appear to be strongly locked.

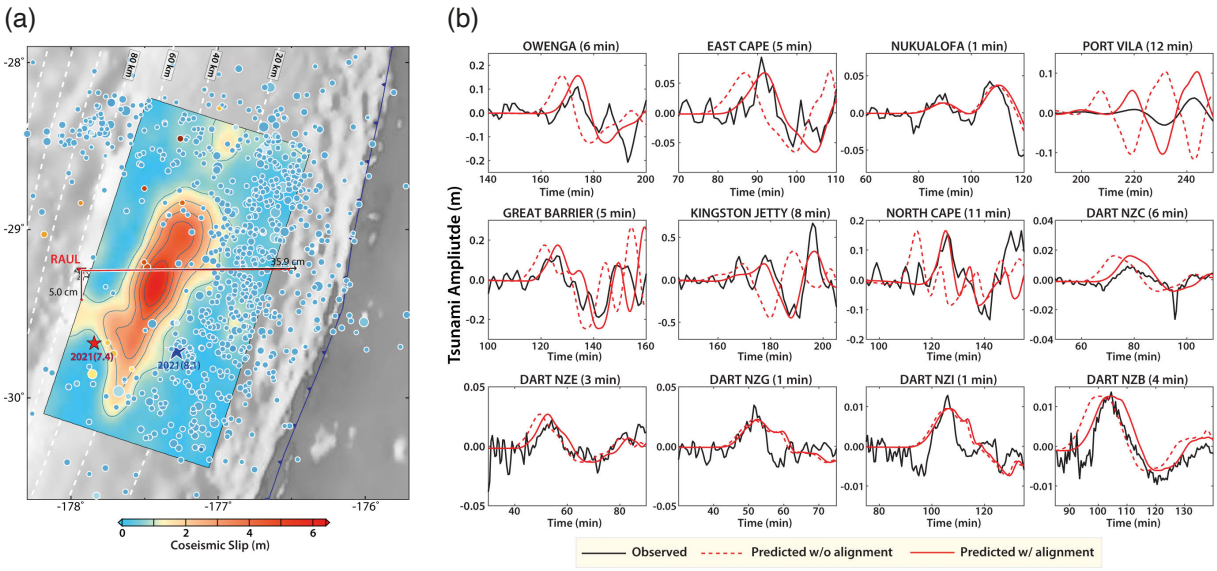

Figure 8. (a) Map view of the finite-fault slip model for the M_W 8.1 Kermadec mainshock from a joint inversion of teleseismic data and displacement at GNSS station RAUL. Red and blue stars indicate the epicenters of the M_W 7.4 and M_W 8.1 events, respectively. Aftershocks within the first 2 months from the USGS-NEIC catalog are shown. Dashed curves indicate the SLAB2 plate interface depth in 20 km increments. The inverted triangle locates GNSS station RAUL, with observed (black) and predicted (red) coseismic displacements. The horizontal and vertical displacements are shown by vectors pointing east and downward, respectively. (b) Waveform fitting of tsunami data to validate the slip model in (a). Black and red lines respectively show observed and predicted tsunami recordings at tide-gauge and DART stations. The station locations are shown in Fig. 1 of Romano et al. (2021). The model predictions are shown without (dashed red lines) and with (solid red lines) time shifts in minutes (indicated at the top of each panel) obtained by cross-correlation alignment.

2.1.4 21 July 2020 Simeonof (M_W 7.8)

The Shumagin seismic gap along the Alaska Peninsula experienced its largest recorded megathrust event on 21 July 2020 when the M_W 7.8 Simeonof event ruptured below the Shumagin Islands southwest of and prior to the 2021 Chignik rupture zone (Fig. 2) discussed in Section 2.1.1. A smaller M_W 7.4 event in 1917 ruptured a portion of the down-dip region of the 2020 rupture. Regional strong-motion and high-rate GNSS data, several of which were on Shumagin Islands overlying the rupture zone, were inverted for slip distributions by Crowell and Melgar (2020), and jointly with teleseismic and regional seismic data by Liu et al. (2020) (Fig. 9b). Ye et al. (2021b) inverted regional GNSS statics and teleseismic data for a slip model (Fig. 9a), and computed tsunami waveform comparisons at tide gauge and DART stations to demonstrate the viability of their model. Xiao et al. (2021) included floating InSAR deformation of the islands, finding a basically similar model to those of Liu et al. (2020) and Ye et al. (2021b), with the inclusion of teleseismic data extending slip futher westward than in the model of Crowell and Melgar (2020). These models indicate predominantly southwestward unilateral rupture expansion. They all have minor slip near the epicenter, which lies adjacent to or within the subsequent 2021 Chignik rupture area, and peak slip of from 2 to 4 m under the Shumagin Islands, with ~1 m slip in the patch to the west. None of these inversions indicate coseismic slip of the up-dip portion of the megathrust at depths less than 20 km. The patchy slip is consistent with the relatively low slip deficit on the megathrust beneath the islands indicated by the overlying geodetic stations (e.g., Li and Freymueller, 2018; Drooff and Freymueller, 2021; Zhao et al., 2022).

The tsunami signals from the 2020 Simeonof event were analyzed by Mulia et al. (2022a), who confirmed that the very long-period signals recorded at regional DART stations constrain the rupture area to depths of 20-40 km. The overlying flat continental shelf has a mean water depth of ~200 m, similar to that along the 2021 Chignik rupture zone. A slip model was obtained by first inverting for the initial vertical sea surface displacement and then inverting that for a finite-fault slip distribution. The tsunami data provide an accurate estimate of up-dip limit of slip, but the large-slip region under the islands is not well-resolved. To achieve a model consistent with the seismic, geodetic, and

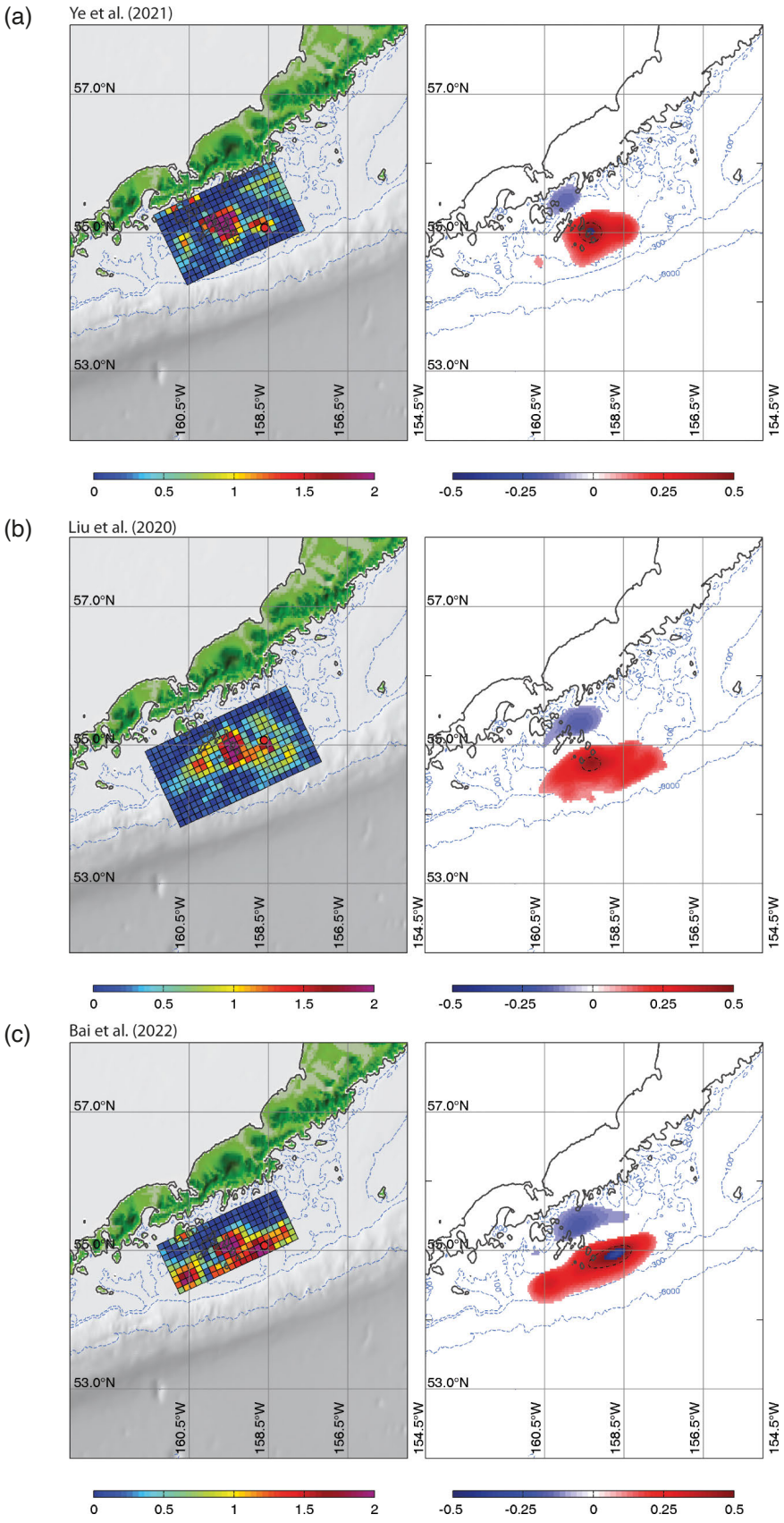

Figure 9. Starting and final slip models for the 2020 Simeonof, Alaska Peninsula earthquake. (a) Slip distribution (left) and vertical seafloor deformation (right) for the starting model from Ye et al. (2021b). The star indicates the hypocenter from an initial USGS-NEIC location (55.325°N, 157.841°W, 32.2 km deep). (b) Slip distribution (left) and vertical sea floor deformation (right) for the starting model from Liu et al. (2020). (c) Slip distribution from the iterative model that matches seismic, geodetic, and tsunami observations well. Modified from Bai et al. (2022).

tsunami observations, Bai et al. (2022) performed an iterative adjustment of the finite-fault inversion of teleseismic, regional broadband and strong-motion seismic, regional GNSS statics, and regional hr-GNSS waveforms of Liu et al. (2020) to improve the fit to tsunami observations (Fig. 9c). This procedure, similar to that described above for the 2021 Chignik earthquake (Section 2.1.1), demonstrates that the optimal model, which best fits the arrival time and amplitude of the first tsunami arrivals at DART and Hawai'i tide gauge stations, has slip located intermediate to the models of Ye et al. (2021b) and Liu et al. (2022) (Fig. 9), with seafloor coseismic deformation located landward of the shelf break. The somewhat too landward position of the slip in the model of Ye et al. (2021b) produces slightly late and underestimated first tsunami arrivals, while the too seaward position of the slip in the model of Liu et al. (2022) produces slightly early and overestimated first tsunami arrivals. The intermediate placement of slip in the preferred model fits the tsunami timing and amplitude well, along with correctly matching multiple coastal reflections. Absolute slip location is resolved within about 20 km accuracy for the combined data set, and there was no shallow coseismic slip. This has been confirmed by observations at a GNSS_a site seaward of the rupture zone by DeSanto et al. (2023). Again, the tsunami data provide tight constraint on the up-dip limit and precise placement of coseismic slip.

2.1.5 10 February 2021 Loyalty Islands (M_W 7.7)

The southern end of the Vanuatu subduction zone has a strong hook, curving around the southwest corner of the North Fiji basin to connect eastward to the Hunter fracture zone. Strong slip partitioning occurs in this region,

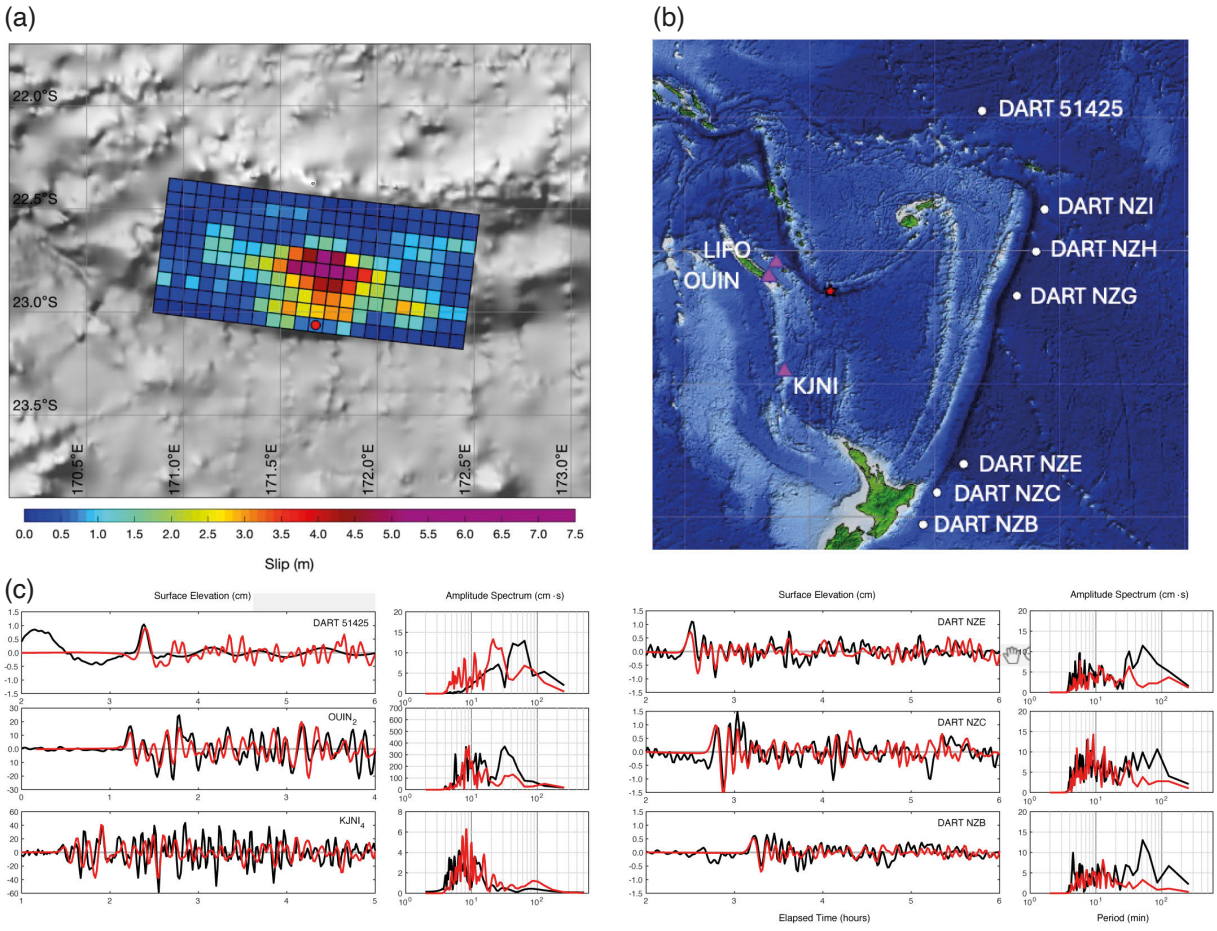

Figure 10. (a) Slip model for the 2021 Loyalty Islands megathrust earthquake from inversion of teleseismic body wave data constrained with iterative modeling of tsunami recordings. The strike is 276.9°, dip is 17.0°, and up-dip edge of the fault is 6.8 km below sea level, with 6.0 km water depth in the trench. The red star is the epicenter. (b) Bathymetry model and locations of tide gauge (triangles) and DART sensors (circles) used in the tsunami modeling. The red star is the epicenter. (c) Observed (black lines) and model predictions (red lines) of a subset of the tsunami signals. Modified from Robert et al. (2024).

as evidenced by the 10 February 2021 M_W 7.7 megathrust event that involves north-dipping trench-perpendicular thrust faulting beneath an upper plate sliver that has left lateral strike-slip faulting on its northern margin (e.g., Roger et al., 2023). The north-south convergence rate of about 45 mm/yr seaward of Matthew and Hunter islands had produced relatively minor seismicity and had uncertain slip deficit prior to the 2021 event. This event is the largest recorded megathrust rupture in the region, although there are comparable size outer rise normal faulting events nearby (see Section 2.3.2). A finite-fault model was obtained by inversion of teleseismic signals by Ye et al. , (2021a), confirming almost pure thrust motion on a northward dipping plane, with slip concentrated at depths from 10 to 22 km. Gusman et al. (2022) inverted tsunami recordings from numerous coastal gauges and New Zealand DART sensors, providing good resolution of shallower faulting, finding concentrated slip of up to 4.1 m near the trench. Tsunami alignments for coastal gauges were made using a procedure like that of Romano et al. (2016), as the bathymetry around many stations is complex and poorly known. Calculations of regional long-period seismic waves were used to validate the model, favoring a low rupture velocity of 1.0 km/s. Joint analysis of seismic and tsunami observations supports strong slip extending up to the trench (Robert et al., 2024), but the source does not appear to be a typical tsunami earthquake (Fig. 10), possibly due to a lack of shallow sediments. Roger et al. (2023) computed tsunami for uniform and non-uniform slip models (Gusman et al. 2022), as well as the USGS-NEIC finite-fault model, and considered tsunami calculations for larger possible earthquakes up to M_W 8.2 along the megathrust. For this event, the tsunami observations play an important role in defining slip extending to near the trench (which is not uniquely resolved by teleseismic data and there are no local GNSS observations), and given the lack of prior large earthquakes in the southern zone, these signals establish the complex path variability and signal characteristics that advance tsunami hazard assessment across the region (Gusman et al., 2022; Roger et al., 2023; Robert et al., 2024).

2.2 Tsunami Earthquakes

A special class of large megathrust ruptures that are strongly tsunamigenic includes very shallow faulting near the trench beneath the toe of the overriding plate. Such events are labeled tsunami earthquakes (e.g., Kanamori, 1972; Polet and Kanamori, 2000; Bilek and Lay, 2002) because the resulting tsunami is larger than expected for a seismic magnitude measured at a period shorter than the unusually long source duration. The shallow portion of the plate contact tends to be very rough due to seamounts and horst and graben structures on the incoming plate, and any overthrust sediments are likely relatively weak and deformed. As a result, conventional models suggested that aseismic stable sliding was the likely mode of convergence (e.g., Byrne et al., 1988; Scholz, 1998). However, in some regions, the shallow megathrust has ruptured spontaneously in very large tsunami earthquakes such as the 1992 Nicaragua M_W 7.7, 2006 Java M_W 7.8 and 2010 Mentawai M_W 7.8 events (e.g., Kanamori and Kikuchi, 1993; Ammon et al., 2006; Yue et al., 2014b; Li et al., 2016a; Lorito et al., 2016) or as part of a rupture that initiated with large slip deeper on the megathrust like the 2011 Tohoku event (Yamazaki et al., 2018; Lay, 2018). The observed low rigidity of the sedimentary wedge (Bilek and Lay, 1999; Sallarés and Ranero, 2019; Sallarés et al., 2021) has been suggested as a cause of large slip at shallow depth and slow rupture velocity, and this has been demonstrated to successfully model depth-dependent tsunami excitation for many large events (e.g., Cheung et al., 2022), while corresponding depth-varying upper plate properties can account for observed rupture characteristics of tsunami earthquakes (e.g., Prada et al., 2021).

Tsunami earthquakes are relatively infrequent, and only one moderate size event has been documented since the review by Romano et al. (2020a). This is the 18 November 2022 Sumatra earthquake that occurred seaward of the rupture zone the 2007 Bengkulu M_W 8.4 megathrust rupture along Southern Sumatra. The 2022 event was initially estimated to have a moment magnitude, M_W 6.9, but that estimate is for a standard reference earth model structure (PREM). Sriyanto et al. (2023) found that lowering the near-source rock rigidity improved the fit to tsunami signals at 4 regional tide gauge stations. Xia et al. (2024) found that reduction of the source velocity structure and associated rigidity at shallow depth is required to reconcile the seismic and tsunami observations for the event (Fig. 11), and the corresponding increase in seismic moment raises the magnitude to M_W 7.3. While the tsunami was modest (~20 cm measured at Seblat tide gauge, western Sumatra), the event has the primary attributes of a tsunami earthquake (low rupture velocity and relatively large slip at shallow depth near the trench).

The 2022 Sumatra event, like the nearby 2010 Mentawai earthquake, occurred as spontaneous rupture of the shallow megathrust up-dip of a prior larger earthquake on the deeper megathrust. This demonstrates the concern for tsunami earthquake ruptures occurring seaward of other deeper megathrust ruptures such as the 2021 Chignik and 2020 Simeonof ruptures. The shallow megathrust between the 2010 Mentawai and 2022 Sumatra events appears

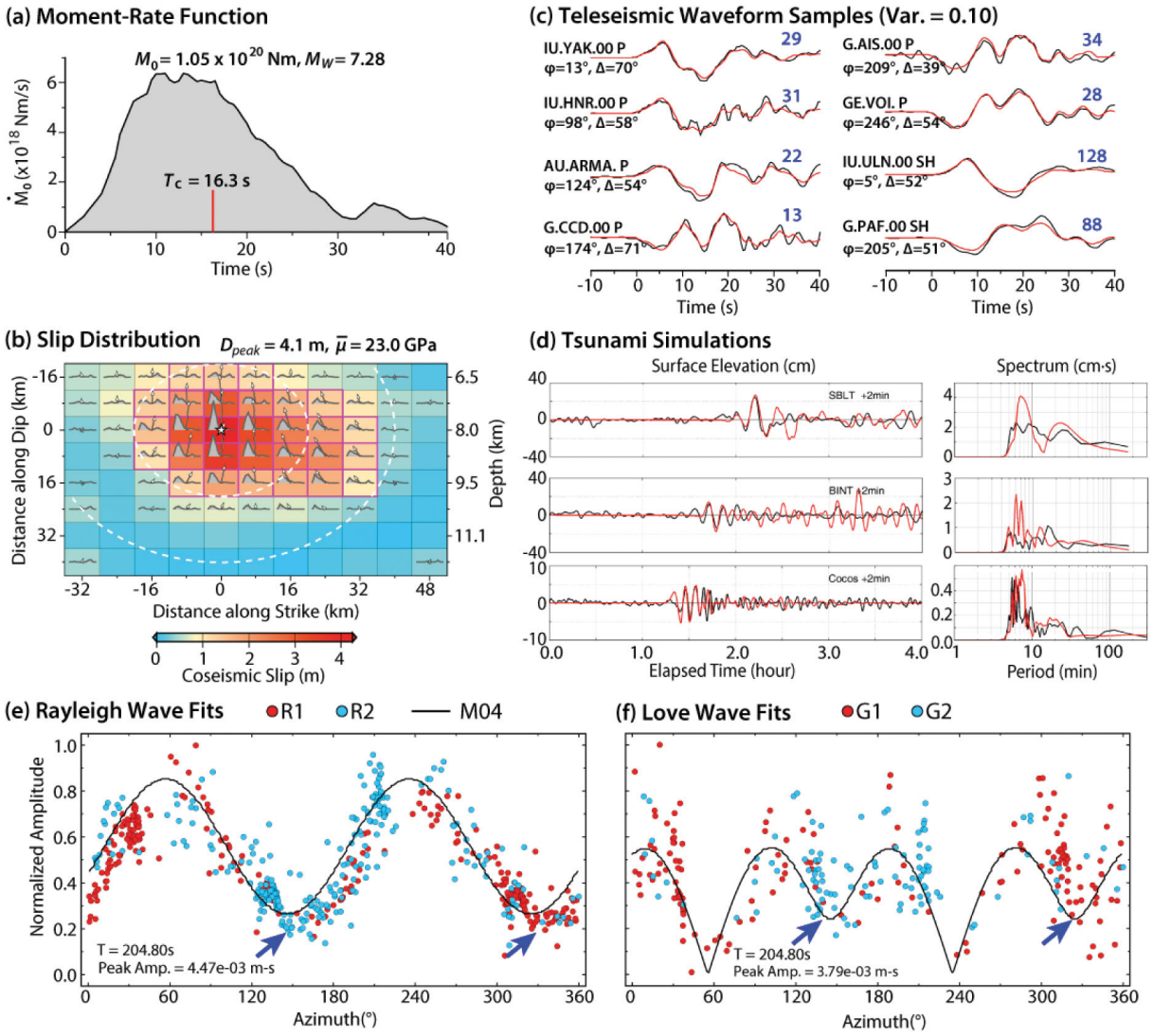

Figure 11. Slip model for the 2022 Sumatra earthquake from inversion of teleseismic body wave data constrained with iterative modeling of tsunami recordings and long-period surface wave spectra. (a) Moment rate spectrum for the final model. (b) Slip distribution on the fault extending downward from the trench along a dip-varying megathrust. (c) Examples of teleseismic P and SH waveform fits for the slip model in (b). Data are shown with black lines, predictions are red lines. (d) Local tide gauge recordings and spectra (black lines) and model predictions (red lines) for the slip model in (b). (e) Observed 204.8 s period Rayleigh wave spectral amplitudes (colored circles) and predictions for the model in (b). (f) Observed 204.8 s period Love wave spectral amplitudes (colored circles) and predictions for the model in (b). Arrows indicate the Love wave radiation asymmetry indicating shallow dip. From Xia et al. (2024).

to have released strain by aseismic afterslip following the 2007 Bengkulu rupture, indicating a patchy distribution of strain accumulation along the trench. Seafloor geodesy measurements appear to be the most promising approach to mapping such strain accumulation to anticipate where tsunami earthquakes may or may not occur.

2.3 Intraplate Earthquakes

Large intraplate earthquakes within shallow oceanic lithosphere can be tsunamigenic, and several important recent events have produced tsunami observations that have contributed to resolving their source processes. The recent examples have all happened nearby or within subduction zones, so they have been well-recorded by DART stations and by tide gauges.

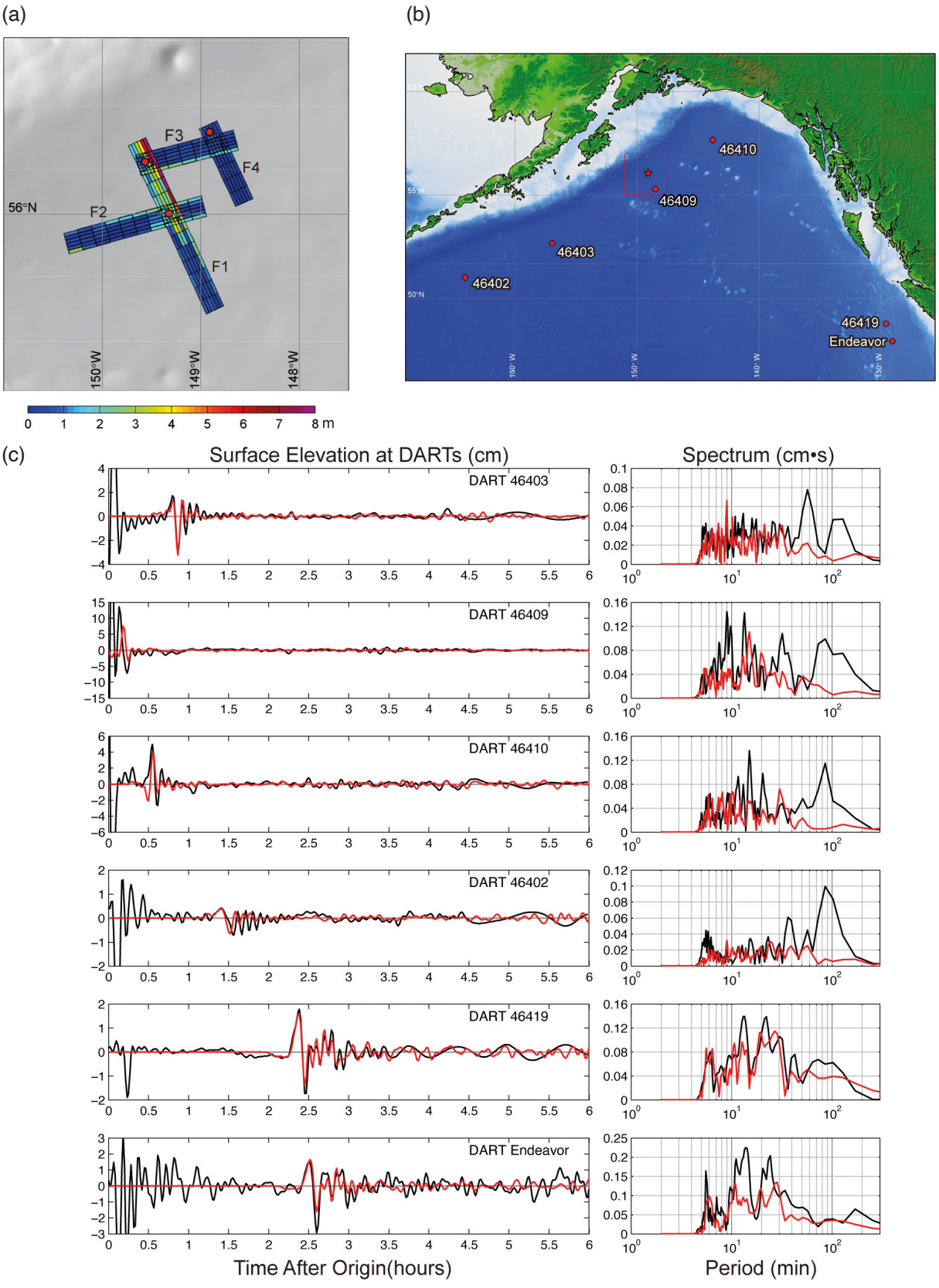

Figure 12. (a) Four-fault slip model for the complex 23 January 2018 Gulf of Alaska earthquake obtained by Lay et al. (2018b) from inversion of teleseismic body waves and regional GPS recordings, along with forward modeling of tsunami signals at DART stations. (b) Bathymetry used in the tsunami modeling and locations of the epicenter (red star) and DART stations used in the modeling (red circles). (c) Comparison of observed tsunami recordings and spectra at DART stations (black lines) with predictions (red lines) for the rupture model in (a). Modified from Lay et al. (2018b).

2.3.1 23 January 2018 Gulf of Alaska (M_W 7.9)

A complex intraplate rupture occurred in the Pacific plate seaward of Kodiak, Alaska on 23 January 2018. The M_W 7.9 Gulf of Alaska earthquake appears to have ruptured multiple faults (Fig. 12), involving four to five nearly orthogonal northwestward and northeastward strike-slip geometries (e.g., Krabbenhoeft, et al., 2018; Lay et al., 2018b; Ruppert et al., 2018; Zhao et al., 2018; Wen et al., 2019). The faulting complexity is a smaller scale version of the great earthquake sequence in the Wharton Basin in 2012 (e.g., Hill et al., 2015). Despite involving largely strike-slip displacements, the event was tsunamigenic, with tsunami waves detectable throughout the Pacific Ocean at open-ocean sites and coastal tide gauges (Wang et al., 2020). While aftershock distributions and teleseismic observations, along with distant on-land geodetic observations, play primary roles in defining the faulting complexity, the modeled tsunami observations include nearby DART stations that provide some resolution of the distributed faulting, as shown in joint modeling by Lay et al. (2018b) and in tsunami-only inversions by Hossen et al. (2020).

2.3.2 18 May 2023 Loyalty Islands (M_W 7.7)

A normal faulting earthquake in the outer rise off the southern Vanuatu subduction zone (Fig. 13) occurred just west of the M_W 7.7 thrust event of 10 February 2021 (Section 2.1.5, Fig. 10). The north-south dipping mechanism

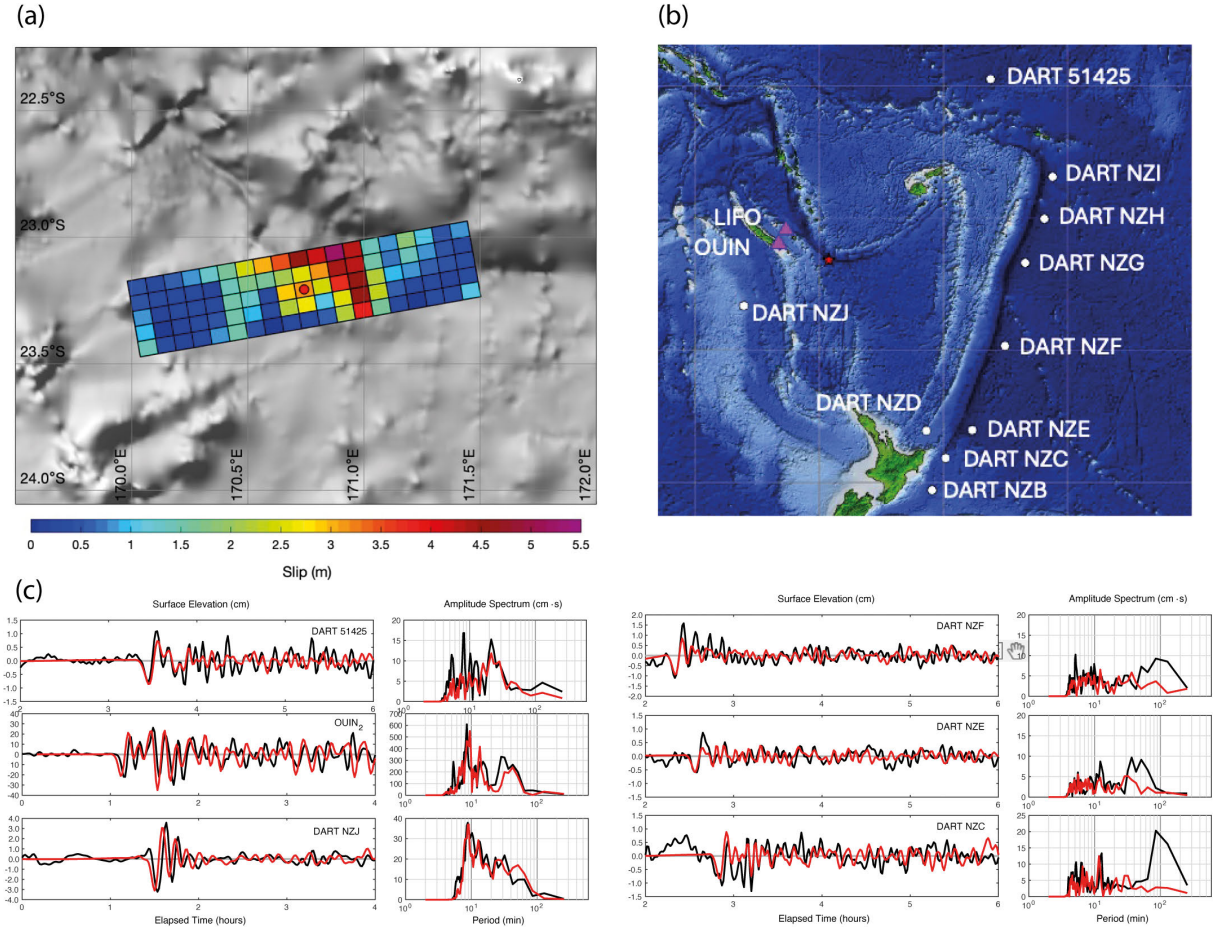

Figure 13. (a) Slip model for the 2023 Loyalty Islands outer rise normal-fault earthquake from inversion of teleseismic body wave data constrained with iterative modeling of tsunami recordings. The strike is 80.0°, dip is 17°, and up-dip edge of the fault is just below the ocean floor. The red star is the epicenter. (b) Bathymetry model and locations of tide gauge (triangles) and DART sensors (circles) used in the tsunami modeling. The red star is the epicenter. (c) Observed (black lines) and model predictions (red lines) of a subset of the tsunami signals. These can be compared with the results for the 2021 megathrust event in Fig. 10 to evaluate the influence of faulting mechanism and precise location. Modified from Robert et al. (2024).

produced similar tsunami radiation pattern (flipped in polarity) and comparable tsunami path complexity to the nearby thrust event. Joint modeling of seismic and tsunami observations (Fig. 13) confirms that most slip occurred within the oceanic crust (Robert et al., 2024). The tsunami recordings for this event are helpful for resolving the depth extent of intraplate rupture and for providing a test of influence of nearby event faulting type and interaction with near-source bathymetric structures (seamounts and small islands) on the tsunami hazard north of the event.

2.3.3 19 October 2020 Sand Point intraplate (M_W 7.6-7.7)

A major M_W 7.6 earthquake struck 80 km southwest of the 21 July 2020 M_W 7.8 Simeonof event (Section 2.1.4) on 19 October 2020, with a predominantly strike-slip moment tensor (Herman and Furlong, 2021; Jiang et al., 2021; Wan et al., 2022; Zhou et al., 2022; Bai et al., 2023). This intraplate rupture is often called the Sand Point earthquake. It is an unusual example of a large strike-slip event with slip primarily concentrated in the subducting slab rupturing seaward of a large megathrust event. Herman and Furlong (2021) and Wan et al. (2022) have considered how variations in the along-strike coupling on the megathrust may influence intraplate stresses, with weak coupling in the Shumagin gap relative to stronger coupling in the Semidi segment to the northeast. However, shallow coupling appears to be quite weak to the northeast as well (Section 2.1.1), so these ideas need to be reconsidered. While seismic and geodetic observations can be well-explained by conventional rapid slip faulting, albeit with two intraplate faults (Wan et al., 2022) one of which may be in the upper plate crust (Bai et al., 2023), such models fail to account for the tsunami observations (Fig. 14a-c).

Bai et al. (2023) show that the tsunami waves from the Sand Point earthquake are stronger than those for the Simeonof event, despite the larger size and thrust-faulting geometry of the latter event. This poses a bit of a mystery given how well the predominantly strike-slip rupture models for the Sand Point event can match the observed seismic and geodetic observations. The possibility of slow slump, slow megathrust rupture, slow rupture of an intraslab fault, or slow rupture of an upper plate crustal fault as sources of the unaccounted for tsunami signals were explored by Bai et al. (2023); in that study the constraint is that any such faulting must not produce nearby ground displacements that violate the observations and do not produce seismic waves in disagreement with the regional and teleseismic observations. While this is a rather ill-posed problem, a viable model was found for a 5 minute long, 15 m slip on a crustal thrust fault with dip semi-parallel to the trench near the shelf break. The geomety is such that negligible ground displacement is produced at GNSS stations on the Shumagin islands, while the long-source process generates minor seismic energy at shorter periods. Such a model, in combination with the fast-slipping faulting, fits the seismic, geodetic, and tsunami (Fig. 14d-f) signals very well (Bai et al., 2023). It is, however, a non-unique model, and there is minor overprediction of very long period seismic waves at one of the global stations that is nodal for the fast-slipping component (H. Kanamori, personal communication, 2023), and observations at seafloor GNSS_a station SPT1 located just west of the faulting (B. Brooks, personal communications, 2023), indicate that the along-trench horizontal motion predicted by the model have the correct direction but overpredicts the observation (this can be adjusted by increasing the dip of the thrust faulting or by shifting the location of the faulting somewhat northeast). Further modeling is underway.

Overall, the contribution of the tsunami observations for this event were in demonstrating the inadequacy of conventional seismic and geodetic inversions for generating the observed tsunami signals, revealing a 'stealth' component to the rupture process that would not have been detected otherwise. When the final geometry is resolved by reconciling the recent GNSS_a observation, efforts to understand the along-trench compressional component will be useful.

2.3.4 30 October 2020 Samos (M_W 7.0)

The largest earthquake to strike in the Mediterranean region in decades was the 30 October 2020 Samos M_W 7.0 earthquake in the eastern Aegean Sea, just offshore of the northern coast of Samos Island (Fig. 15). This event involved shallow normal faulting over a length of 30 to 40 km with east-west strike and northward dip of about 35° and up to 3.5 m slip during a ~20 s long, westward propagating rupture, as resolved by seismic and geodetic (GNSS and InSAR) analyses (e.g., Sun et al., 2024; Kiratzi et al., 2022; Plicka et al., 2022; Ren et al., 2022; Taymaz et al.,

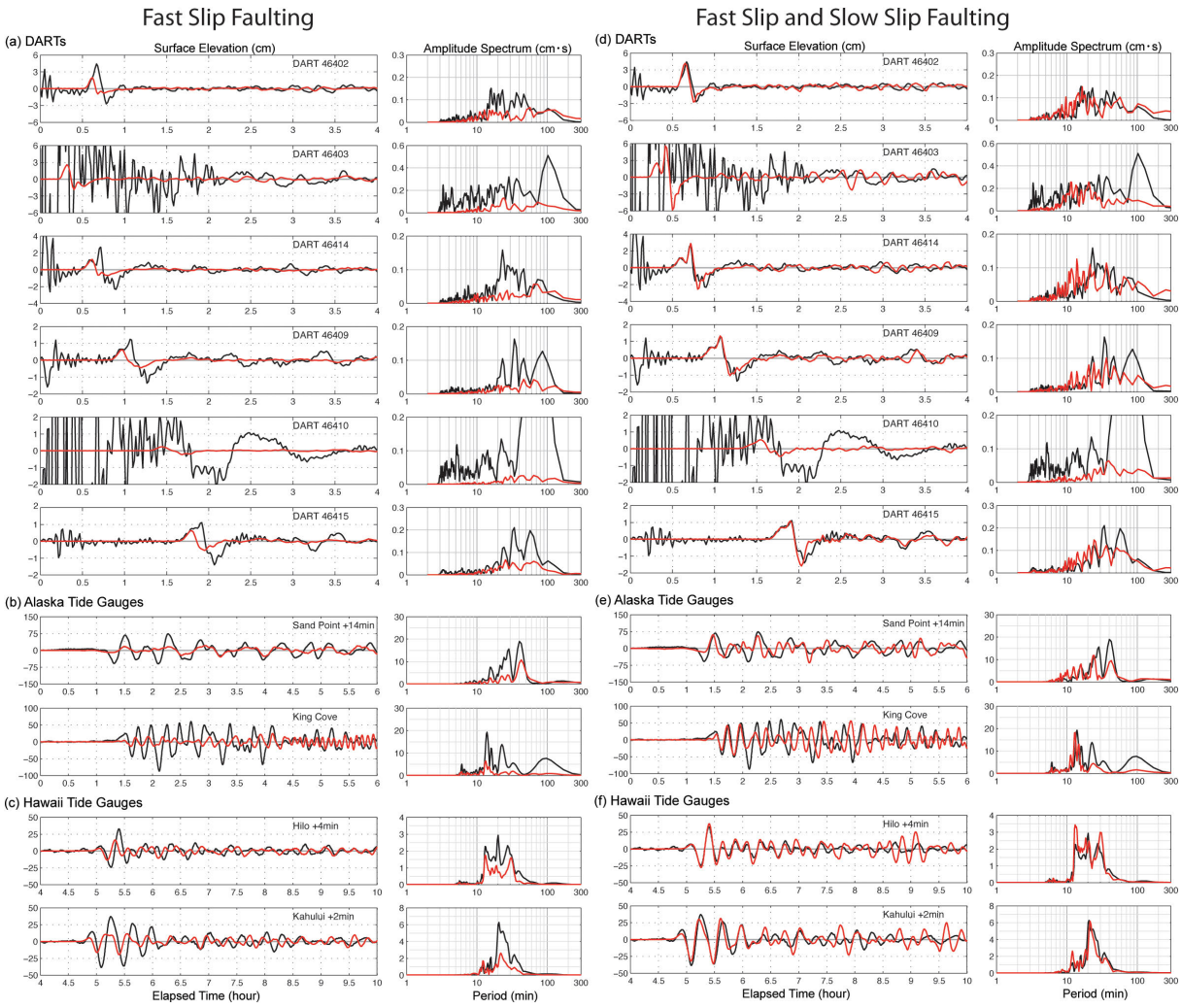

Figure 14. Tsunami predictions at north Pacific DART stations and Alaska and Hawai'i tide gauges for two finite-fault slip models for the 19 October 2020 M_W 7.6-7.7 intraplate rupture seaward of the 2020 Simeonof M_W 7.8 earthquake (Fig. 2). The left column (a)-(c) shows recorded tsunami signals (black lines) compared with predictions (red lines) for an intraslab strike-slip and upper plate oblique normal faulting compound rupture with typical rupture velocities that fits distant and regional seismic and regional geodetic observations very well. However, the model fails to predict the secondary largest tsunami peak in the data at DART stations and underpredicts tide gauge data. Inclusion of large slip on a shallow trench-perpendicular slow slip reverse fault in the upper plate (d)-(f) allows the data to be well matched. The tsunami data reveals a dominant source contribution that was not resolved by seismic and geodetic data analysis. Modified from Bai et al. (2023).

2022; Chousianitis and Konca, 2021; Ganas et al., 2021; Meng et al., 2021, Sakkas, 2021). The north-south extension in this backarc region of the Hellenic subduction zone is generally attributed to upper plate stresses induced by roll-back of the underthrust African plate (e.g., Jolivet et al., 2013; Meng et al., 2021).

The tsunami produced by the earthquake is the largest in the Aegean Sea since 1956 (Hu et al., 2022; Triantafyllou et al., 2021). Heidarzadeh et al. (2021) discuss how the semi-closed basin around the source region produced several basin oscillations, with arrival time of the largest tsunami delayed by up to 14.9 hr after the first arrival, and waves persisted from 18 to 30 hr on 8 regional tide gauges (Sun et al., 2024). Hu et al. (2022) further attribute the tsunami strength to rupture having occurred under the deepest portion of the Samos Basin with the east-west fault orientation focusing tsunami energy northward toward Sigacik Bay, along the Turkish coast, where 3.8 m high waves were observed (Dogan et al., 2021). With the primary tsunami wave period being similar to the natural oscillation frequency of the regional bays, strong resonances were established, but it proves difficult to model the very long persistence of the tsunami signals, likely due to limitations of the regional bathymetry models

(Sun et al., 2024) and the diffraction effects due to the presence of a number of small islands along the propagation path toward the tide gauge locations. Therefore, the measured tsunami signals (less than 10 cm of amplitude at the tide gauges in the Aegean Sea) in this case do not contribute to resolving spatial details of the seismic source. Nevertheless, in non-subduction tectonic frameworks like Samos Island, information about the tsunami first arrival polarities along the coasts help to discriminate between the two nodal planes of the moment tensor (Fig. 15c), in contrast to teleseismic data. Thus, the right fault geometry can be adopted to refine the slip distribution by inverting seismic and/or geodetic data. The tsunami observations in this case both confirmed the northward dipping faulting solution and allowed analysis of the resonance effects produced by the configuration of coastal bays and islands, that will influence tsunami hazard assessments.

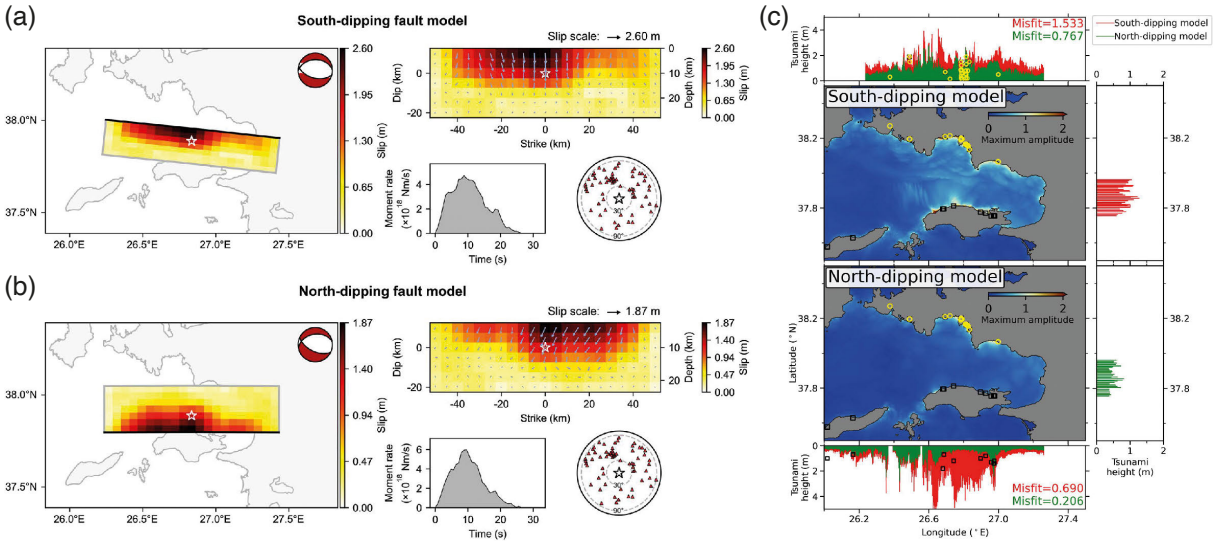

Figure 15. Slip models for the 30 October 2020 Aegean Sea earthquake obtained by Heidarzadeh et al. (2021) based on (a) a south-dipping fault plane (strike/dip angles = 96°/53°), and (b) a north-dipping fault plane (strike/dip angles = 270°/37°). The figure shows the moment-rate function for each case (the gray-shaded plots) as well as the worldwide distribution of the teleseismic data used in the inversion (the earth's map with red triangles). The star represents the epicenter. (c) Comparison of surveyed tsunami heights and run-up data (yellow circles and black rectangles) with computed maximum nearshore tsunami amplitude (peak coastal tsunami amplitude) using the south-dipping fault model (red bars) and north-dipping fault model (green bars) along the coasts of Turkey and Greece for the 30 October 2020 tsunami. The surveyed data are from Dogan et al. (2021) and Triantafyllou et al. (2021). The colormap for the offshore area shows maximum tsunami amplitudes (in meters) at each computational grid point during the entire tsunami simulations. The red and green numbers are tsunami misfits for the south- and north-dipping models, respectively. From Heidarzadeh et al. (2021).

2.4 Hawaiian Décollement Ruptures

The huge volcanic mass of the Island of Hawai'i is superimposed on Pacific Plate seafloor, and large shallow-dipping thrust earthquakes have occurred on the décollement fault in response to ongoing volcanic construction and wedging apart of the island. These events have occurred both simultaneously with volcanic eruptions and in between eruptions.

2.4.1 4 May 2018 Hawai'i (M_W 6.9-7.2)

The 2018 eruption of Kilauea on the island of Hawai'i was a major event with volcanic activity at both the summit, where eruptions and collapse events occurred in the caldera, and along the East Rift Zone where fissures erupted as magma drained from the summit and Pu'u O'o plumbing system (e.g., Anderson et al., 2019). Associated

with the rift zone dike intrusions (Chen et al., 2019), there was a moderate M_W 6.9 earthquake on 4 May 2018 on the basal décollement extending offshore of the northeast part of the rift zone. This earthquake shaking was not seriously damaging, but it generated a modest tsunami recorded at tide gauge stations around Hawai'i. A kinematic finite-fault inversion of teleseismic, strong-motion, and GNSS data resolved a patchy slip distribution along strike with peak slip of about 3.5 m offshore on a 7° landward dipping décollement fault (Liu et al., 2018). A low rupture velocity of ~1 km/s was estimated, although back-projections of teleseismic data suggest some faster surges within the early part of the rupture which has an overall low 1.5 km/s rupture expansion (Kehoe et al., 2019). The Liu et al. (2018) model has a seismic moment of 2.5×10^{19} Nm (M_W 6.9). An iterative procedure of inversion of teleseismic, and nearby GNSS static offsets, along with forward modeling of tsunami recordings at tide gauge and DART stations around Hawai'i provides a slip model (Fig. 16) with dip of 7.5°, with peak slip of 3.8 m within a large-slip patch at depths of 3.7 to 6.4 km just offshore of the Hawaiian coast (Bai et al., 2018). The seismic moment is 8.69×10^{19} Nm (M_W 7.2) with slip spread broadly over the offshore décollement. Modeling of long-period Rayleigh and Love wave spectra indicates that the décollement dip is in the range 2.5° to 7° (Lay et al., 2018a). Decreasing the fault dip to 3° results in a slip model with large slip concentrated down-dip just off the coastline and a seismic moment estimate of 7.5×10^{19} Nm (M_W 7.2), albeit with minor reduction in fit of the teleseismic and GNSS observations (Lay et al., 2018a). Chen et al. (2019) obtain a similar offshore slip model from inversion of teleseismic, strong motion, and GPS static offset data for a dip of 5°, with seismic moment of 7.31×10^{19} Nm (M_W 7.2), so there is fairly consistent estimation of $M_W = 7.2$ for this event. In this case, the tsunami data help to bound the strong tradeoff of slip and seismic moment with dip for the shallowly dipping décollement fault. Being the largest offshore thrust event since the 1975 Kalapana M_W 7.7 earthquake along the same coastline (discussed below), the modeling of the tsunami recordings across the Hawaiian Islands also informs tsunami hazard assessment for the active volcanic margin.

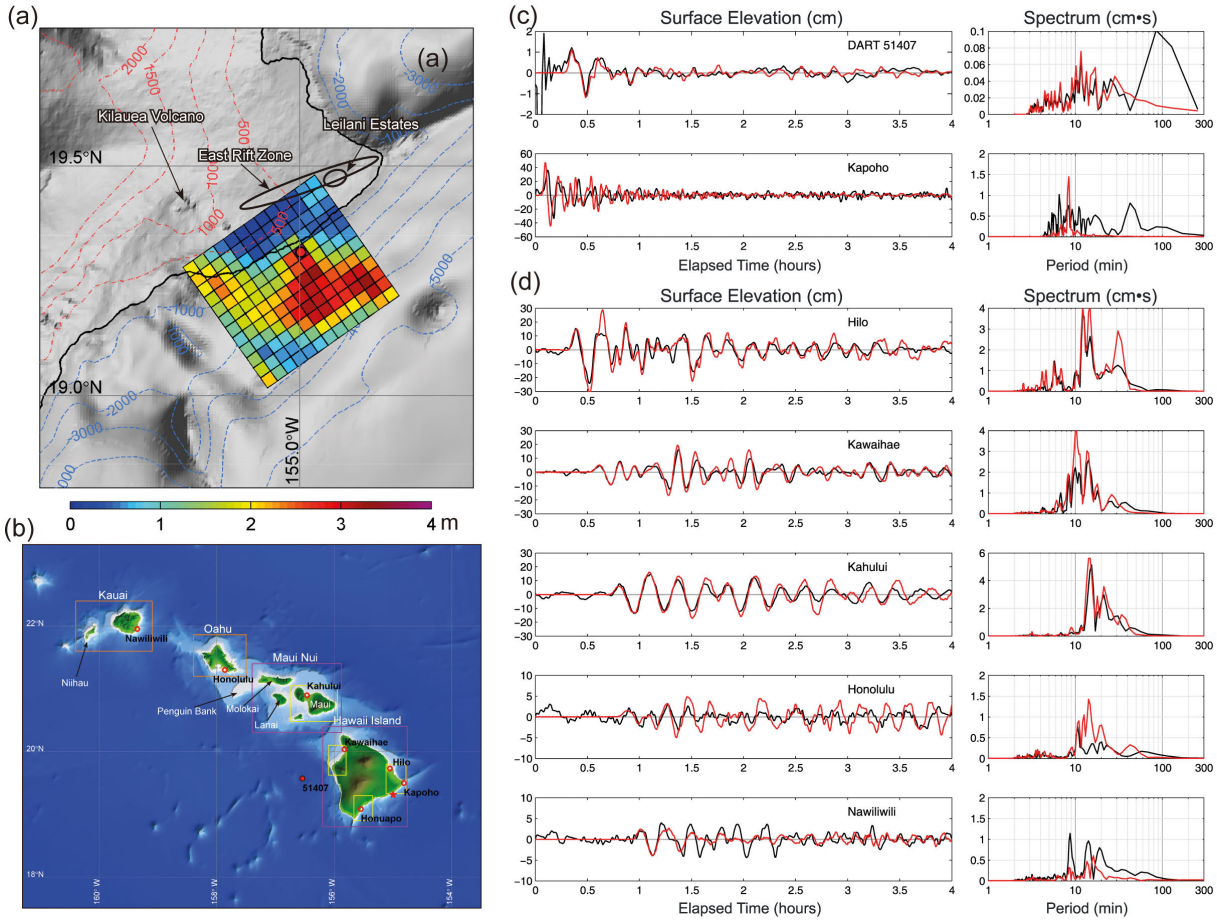

Figure 16. (a) Décollement slip for the 4 May 2018 earthquake during the 2018 eruption of Kilauea (Bai et al., 2018). (b) Locations of tide gauge and DART stations around Hawai'i that recorded the tsunami from the earthquake. (c) The comparisons of observed tsunami recordings and spectra (black traces) with model predictions for the slip model in (a) are shown for DART sensors (c) and tide-gauges (d). From Bai et al. (2018).

2.4.2 29 November 1975 Kalapana (M_W 7.7)

The 29 November 1975 Kalapana M_W 7.7 earthquake along the southeastern coast of Hawai'i produced peak runup of at least 14.3 m on the shore adjacent to Kilauea, comparable to that produced by the great 1868 Ka'u earthquake along-shore to the southwest. Onshore normal faulting occurred along the Halina fault, and there was likely some offshore block slumping. Decreasing geodetic coseismic deformation was measured along the coast from 155.4°W to 154.4°W (Lipman et al., 1985), spanning the region ruptured by the 2018 décollement faulting described in Section 2.4.1 (Fig. 16). Various models for the event have been produced from seismic waves, geodetic deformation and tsunami observations at tide gauges around Hawai'i (e.g., Ando, 1979; Furumoto and Kovach, 1979; Eissler and Kanamori, 1987; Ma et al., 1999; Nettles and Ekström, 2004; Day et al., 2005; Owen and Bürgmann, 2006). However, no consensus on the overall source process had been achieved.

The geodetic measurements and tsunami tide gauge recordings (~80 cm of amplitude at Hilo, ~40 cm Kahului, and ~10 cm at Honolulu) and runup observations (Fig. 17) were modeled to determine slip distributions on both the offshore décollement and a shallow crustal block-faulting system extending from the Halina fault outcrop to offshore by Yamazaki et al. (2021). Slip variations for a 7 subfaults representation of the two main fault systems (3 rectangular planar subfaults along the décollement and 4 rectangular planar subfaults for the shallow block-faulting, each with uniform slip) were determined by extensive forward modeling that matches the suite of data quite well. Localized details of the slip distribution and effects of some likely localized coastal slumping are not resolved with the parameterization used. The 4°-dipping décollement slip varies from 8 to 4.5 m, across 10 km width extending 58 km along the coast. The up-dip portion of the décollement does not have coseismic slip, in contrast to a geodetic model produced by Owen and Bürgmann (2006), and this is supported by the tsunami observations. The lower slip region is overlapped by the 2018 M_W 7.2 rupture discussed in Section 2.4.1. The shallow block faulting has 4 m of slip at the surface and up to 10 m on a 3° landward dipping mid-crustal fault.

The role played by the tsunami observations for this source characterization are central; run-up contributions from the Hilina block-faulting and the décollement faulting are found to be comparable along the coast, and the compound faulting accounts for the localized peak values exceeding 10 m well (Fig. 17d). The tide gauge signals are more strongly generated by the décollement faulting due to the larger source region relative to the near-coast block faulting (Fig. 17c). Future analysis including seismic body wave observations might be able to provide timing control on the rupture expansion; the modeling done by Yamazaki et al. (2021) assumed synchronous rupture.

2.5 On-shore/off-shore Ruptures

Some large earthquakes occur on land margins, with slip both under land and under water, such as the 16 November 2016 M_W 7.8 Kaikoura, New Zealand and 28 September 2018 M_W 7.5 Palu, Sulawesi strike-slip earthquakes, both of which generated tsunami (see discussions in Romano et al., 2020a). The tsunamis for such events can be both very damaging, notably for the 2018 Palu event, and valuable for constraining the offshore component of slip, including deeper megathrust contribution, as for the 2016 Kaikoura event.

2.5.1 1 January 2024 Noto Peninsula (M_W 7.5)

An important recent example of rupture traversing the coastline is the 1 January 2024 Noto Peninsula M_W 7.5 reverse faulting earthquake in western Honshu, Japan. This shallow crustal event initiated above a deeper earthquake swarm with more than 20,000 events with magnitudes less than 5 that commenced in November 2020 (e.g., Amezawa et al., 2023; Yoshida et al., 2023; Kato, 2024). Fluids rising from the region of the swarm may have weakened the crustal fault leading to several larger events with M_W 5.1 in 2022 and M_W 6.2 in 2023, prior to the M_W 7.5 event in 2024. There is extensive geophysical instrumentation along the west coast of Honshu and the event was very well recorded by GNSS stations on the peninsula, regional strong-motion stations, InSAR imagery, and seafloor pressure sensors along with tide gauges. InSAR and seismic data are used by Ma et al. (2024) to develop a finite-fault model, with two main slip patches beneath the peninsula and a weaker slip patch offshore. The offshore slip is not resolved at all by InSAR, so there is intrinsic imbalance in the information along the fault, and only tsunami data can add additional constraints offshore. Masuda et al. (2024) use regional tide gauge recordings

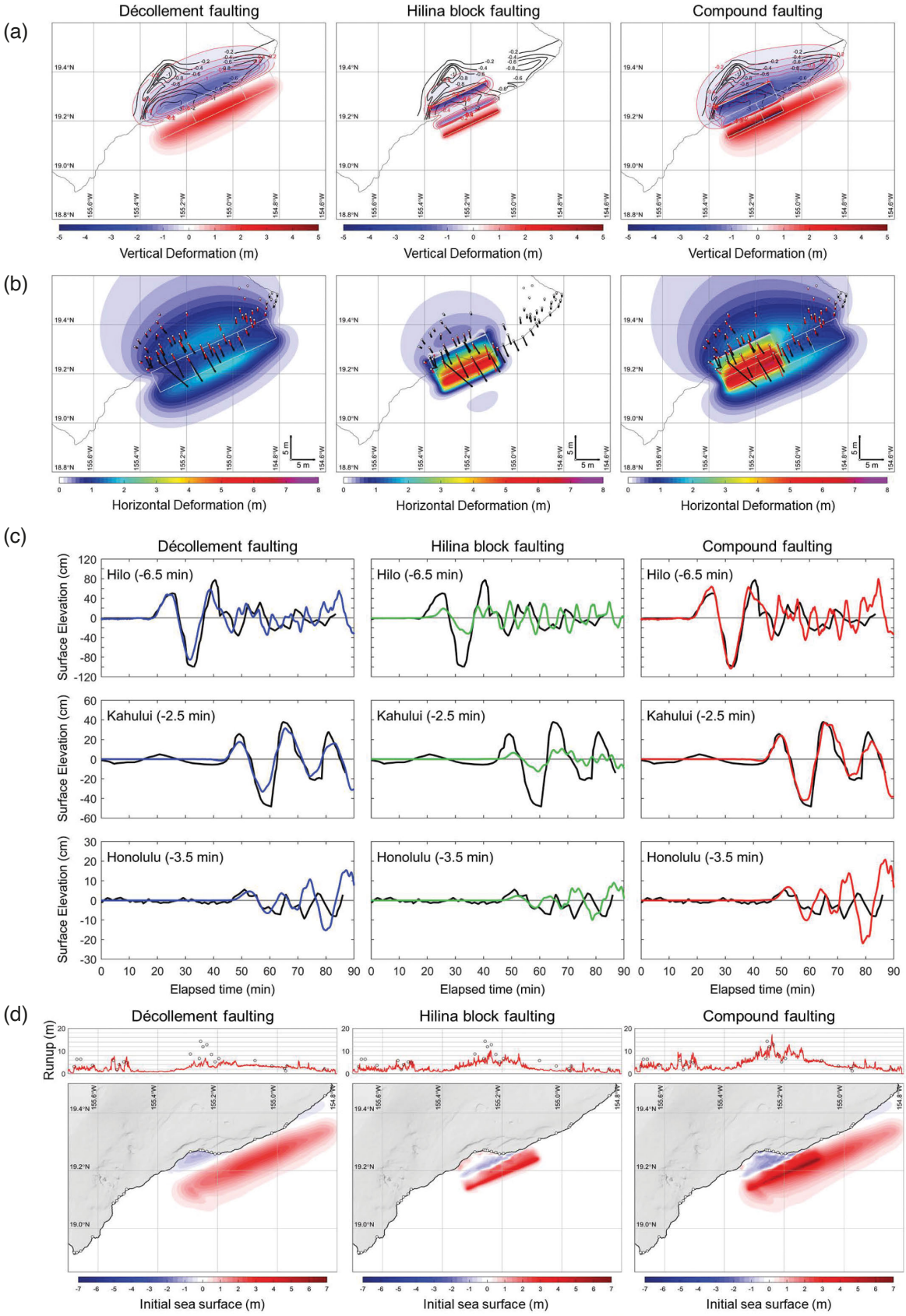

Figure 17. Compound faulting model for the 1975 Kalapana, Hawai'i earthquake, involving slip on the offshore basal décollement (left), in the crustal Hilana block (middle) and composite deformation from both faults (right). (a) Computed and observed vertical deformation. (b) Computed and observed horizontal deformation. (c) Tide gauge data (black traces) and predicted signals (color traces). (d) Initial sea level uplift (lower maps) and comparison of observed runup (circles) and predictions (red curve). Modified from Yamazaki et al. (2021).

to evaluate the tsunami propagation and inundation to help define the offshore faulting system. Liu et al. (2024) performed inversions of teleseismic, regional strong motion, GNSS statics, and InSAR measurements to solve the slip distribution, with forward modeling of tsunami recordings from pressure sensors located outside the complex harbor regions with tide gauges as a guide to weighting of the different data sets (Fig. 18). This is important as separate inversions of seismic data and geodetic data result in bilateral and unilateral ruptures, respectively. The inclusion of tsunami data results in an asymmetric bilateral rupture, with patchy slip offshore and two main patches under the peninsula as found by Ma et al. (2024). Thus, tsunami data are clearly important for balancing the coverage of the geophysical data and need to be considered in modeling this event. Nevertheless, research on this event is ongoing and a recent study exploited the tsunami data (tide gauges, video footage, and tsunami trace heights) to argue that a significant contribution to the tsunami source could be also due to five seismically-induced submarine landslides occurred ~50 s after the Noto earthquake (Yanagisawa et al., 2024).

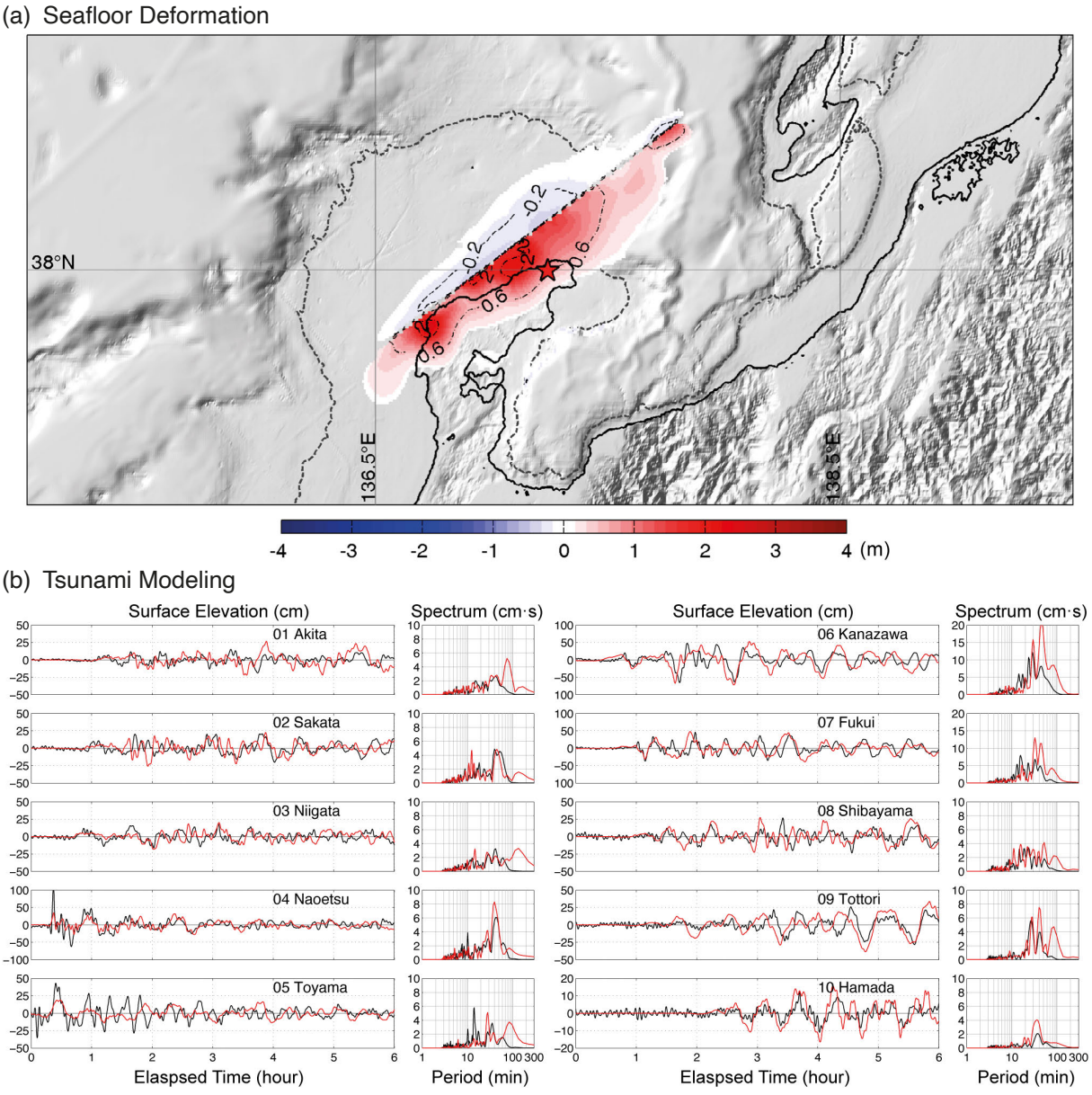

Figure 18. Rupture model for the 1 January 2024 Noto earthquake, which extends offshore from the Noto Peninsula in western Honshu. (a) Vertical seafloor and land surface deformation computed for the Liu et al. (2024) model from inversion of teleseismic, strong motion, GNSS statics, InSAR statics, and iterative modeling of the tsunami data. (b) Comparison of tsunami waveforms and predictions at the seafloor pressure stations along the coast. Black lines represent observed time series (left) and amplitude spectra (right), while the predictions are indicated by red lines. From Liu et al. (2024).

2.5.2 6 February 2023 Türkiye earthquake (M_W 7.8)

While faulting displacement and significant ground displacement was confined to onshore, the 6 February 2023 M_W 7.8 Kahramanmaras rupture on the East Anatolian fault (e.g., Liu et al., 2023b; Gabriel et al., 2023 and many more) produced a weak tsunami at four tide gauges (maximum amplitude of ~15 cm at Hatai and Erdemli) in the eastern Mediterranean Sea (Hu et al., 2023). The event was coincident with a regional cyclone, which dominated sea level motions at some sites (Medvedeva et al., 2023). Hu et al. (2023) and Heidarzadeh et al. (2023) perform back-tracking of the tsunami arrivals and attribute the tsunami excitation inside Iskenderun Bay to landslide movements near the Iskenderun port (Fig. 19), and Hu et al. (2023) attribute tsunami outside the Bay to liquefaction in the coastal plains of Antakya. Dynamic shaking from the earthquake triggered these failures. This is an example of unusual source excitation of tsunami, similar to prior Mediterranean occurrences along the Dead Sea system and in the Black Sea along the northern Anatolian fault. Rapidly retrieving information about such events is relevant because they are challenging to account for in tsunami hazard assessment, and even more for tsunami warning systems, as they may trigger a major alert because of their magnitude, followed by a non-damaging tsunami due to the mainly horizontal fault movement. The Türkiye earthquake, in particular, triggered a basin-wide tsunami watch for the Mediterranean Sea, leading to coastal evacuation and train stopping in Italy (Lorito et al., 2023). Transitioning to tsunami warning approaches which consider not only the earthquake hypocentral location and magnitude but also the (uncertain) faulting style, would limit false tsunami alarms for this type of event (Selva et al., 2021).

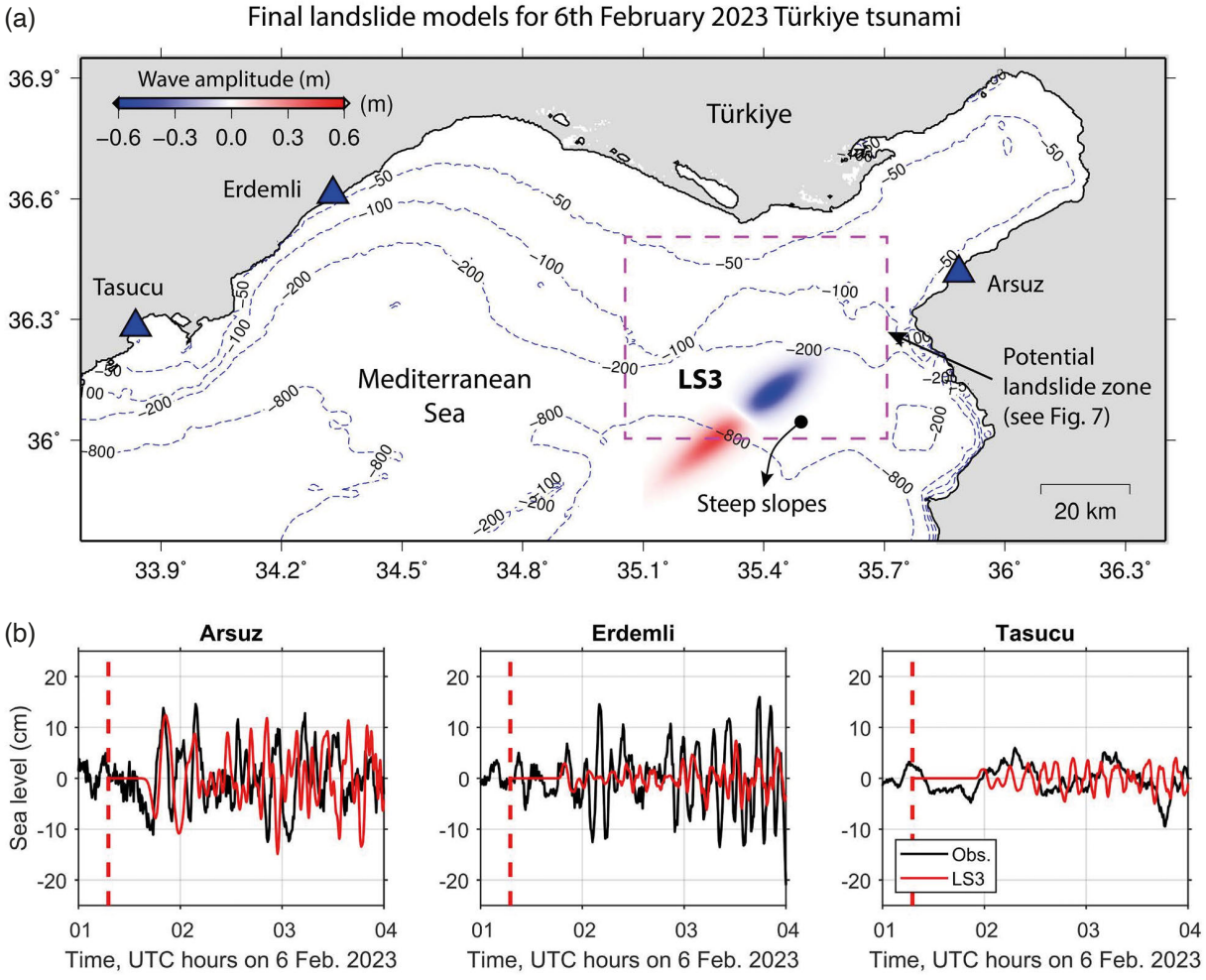

Figure 19. (a) The submarine landslide source model triggered by the 6 February 2023 M_W 7.8 Türkiye on-land rupture of the Eastern Anatolian Fault preferred by Heidarzadeh et al. (2023). The contours are bathymetry in m. (b) comparison of tsunami signals recorded at nearby tide gauge stations (black lines) and predictions for the model LS3. The Dashed lines indicate the earthquake origin time. From Heiderzadeh et al. (2023).

2.6 Historic Eastern Aleutian Islands ruptures

Final demonstrations of the great value of tsunami observations for source modeling presented here are for the subduction zone along the eastern Aleutian Islands in the region of the great 1957 Aleutian M_W 8.7 ± 0.1 megathrust earthquake. In this case runup and inundation observations and tsunami stratigraphic deposits play a critical role in revising earlier estimates of the slip distribution for the 1957 event and in providing models for three pre-seismic events in the eastern Aleutians. The data used are from recent geologic field measurements and boreholes in the Aleutian Islands and Hawai'i, supplemented by many runup measurements documented for the 1957 event (Walker, 2004) that were not previously used to constrain the source. Tide gauge recordings are also modeled for the 1957 event but are not available for earlier events. Reliable modeling of the runup, inundation and stratigraphic deposit observations is enabled using NEOWAVE, as the landward propagation of tsunami from the megathrust faulting can be accurately computed.

2.6.1 9 March 1957 Aleutian (M_W 8.6-8.8)

The great 9 March 1957 Aleutian earthquake had an ~1200 km long aftershock zone and produced major tsunami in Hawai'i, with up to 16.2 m runup at Waihiha Bay, Kaua'i. The event is the second largest to have struck the United States in the last 300 years, but only a handful of seismic stations recorded the event on scale and early inversions for the slip distribution relied on several tide gauge recordings and surface waves from one seismogram (Johnson et al., 1994). The slip models produced using the limited tsunami and seismic data placed most slip in the western 500-600 km of the model, with very little slip in the eastern 700 km, which is surprising given the large run-up observed in Hawai'i (Walker, 2004). About two decades later, field work in the eastern Aleutian Islands documented extensive 1957 tsunami runup and log deposits in Stardust Bay (Sedanka Island), Driftwood Bay (Unmak Island), and along the coastlines of Chuginadak Island (Witter et al., 2016, 2019; Griswold et al., 2019), as well as inundations at Hawaiian sites in Anahola (Kaua'i), Kahana (O'ahu), and Pololu (Island of Hawai'i) (La Selle et al., 2020). Localized tsunami modeling (Nicolsky et al., 2016; Griswold et al., 2019) established that up to 20 m of slip in the eastern portion of the 1957 rupture is required to match the local run-up values of 18 to 32 m on the eastern Aleutian Islands.

To develop a unified source model for the 1957 rupture informed by the recent field observations, Yamazaki et al. (2024a) modified the seismic model proposed by Johnson et al. (1994) for the western portion of the rupture, forward modeling the runup and inundation observations in the Aleutian Islands and Hawaiian Islands with large slip in the eastern portion of the model. Numerical modeling with NEOWAVE established that the most efficient way to generate the very large observed runup of up to 32 m was to have slip concentrated near the trench, producing a narrow initial sea level ridge that would propagate toward land with constructive interference from the landward rebounding sea-level to give enhanced local runup, while propagating seaward with sufficient amplitude to account for the large runup observed in Hawai'i. The favoured model is shown in Fig. 20, with the red zones outlined in white depicting the regions of large slip in the 1957 rupture. The eastern 600 km of the rupture model has from 12 to 26 m of slip (the largest slip is in the red patch outlined in black where a 15th century event ruptured previously (discussed below). This shallow large slip is assumed to have ruptured with low rupture velocity and/or long rise time to avoid strong seismic wave generation, so it is essentially a tsunami earthquake component of the 1957 rupture. The rupture has deeper, typical slip in the western 500 km of the model in Fig. 20 based on the seismic data. Some of the observed and computed runup and inundation observations are shown in Fig. 21 with good fits to data at Driftwood Bay and Stardust Bay, allowing for 1 m flow depth for the drift log deposits, and good prediction of the runup along the coasts in Hawai'i. This rupture model also provides excellent fits to tide gauge recordings in Alaska, California and Hawai'i, so the model appears quite viable as a first-order representation of the faulting, with slip now recognized to be distributed along at least 1100 km of the 1957 aftershock zone.

This example is representative of how robust modeling of tsunami runup and inundation data can provide critical information on nearby offshore faulting, as was shown for the 2011 Tohoku earthquake by Yamazaki et al. (2018). Such modeling is still limited by the resolution of nearshore bathymetry, as seen in Fig. 21 along Wainiha, Kaua'i, where the model locally predicts about 8 m runup, falling short of the locally observed 16.2 m, likely due to very local effects. The runup on the Pacific-facing south side of Chuginadak Island is quite well modeled, but the limited precision of the available bathymetry model prevents accurate modeling of the waves that wrap around to runup on the northern side of the island.

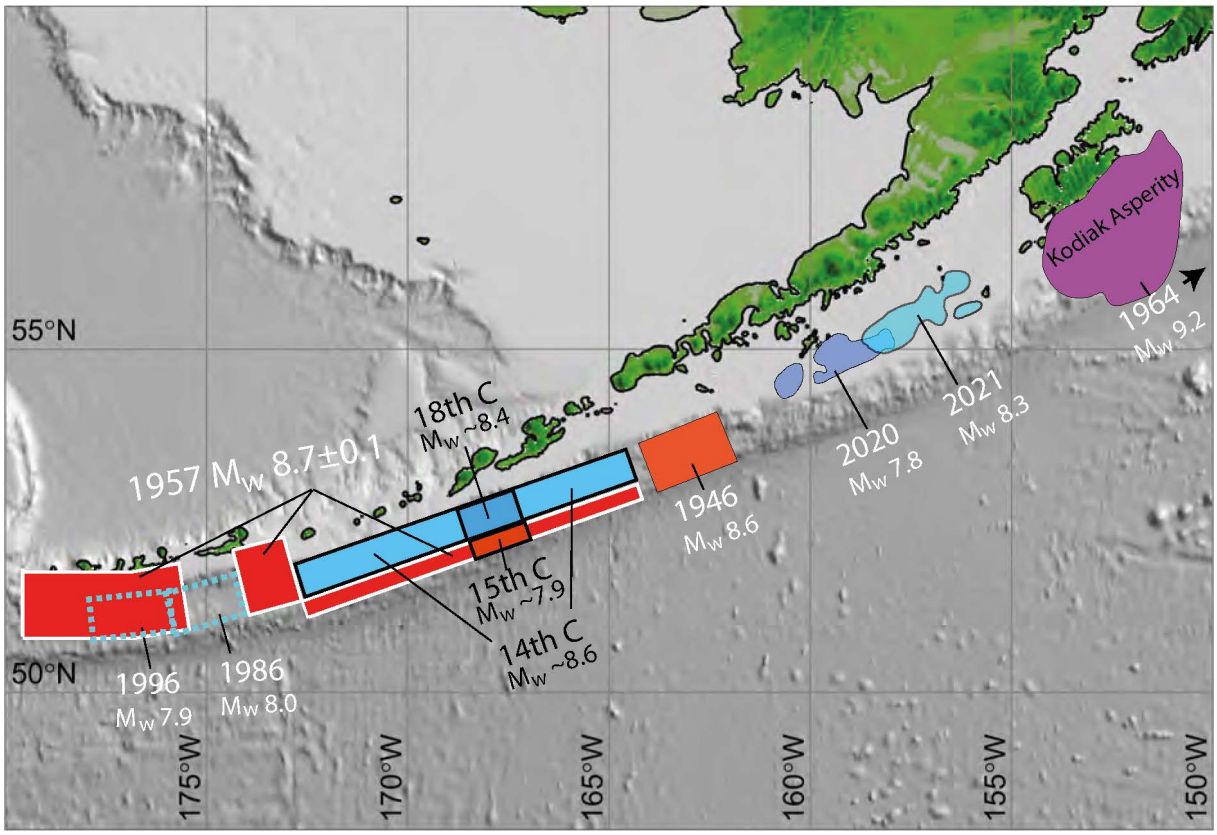

Figure 20. Large-slip zones for major earthquakes along the Aleutian Islands and Alaska Peninsula, updated from the compilation in Yamazaki et al. (2024a). The region of the Kodiak asperity in the western portion of the 1964 Alaska earthquake with slip >4 m is shown in magenta. The 2020 Simeonof and 2021 Chignik source regions have >0.5 and 2 m slip, respectively (Liu et al., 2023a; Bai et al., 2022). The 1946 large-slip zone (8+ m) from López and Okal (2006) is coloured red. The 1986 source region with > ~2 m slip from Boyd and Nabelek (1998) and the 1996 earthquake large-slip zone from Tanioka and González (1998) are outlined in cyan. The red patches with white outline are the updated model for the 1957 M_W 8.8 earthquake from Yamazaki et al. (2024a). Three prehistoric ruptures in the eastern Aleutian Islands determined from tsunami observations in Aleutian Islands and Hawai'i by Yamazaki et al. (2024b) in the 15th century event (outlined in black and overlapping the 1957 shallow slip zone) and 14th and overlapping 18th century events (in blue, outlined in black) ruptured down-dip from the shallow rupture in 1957.

2.6.2 18th, 15th, 14th Century Aleutians

The field deployments in the eastern Aleutian Islands and Hawai'i discussed in the previous section on the 1957 earthquake included stratigraphic sections in shallow cores and exposed stratigraphy, that reveal tsunami deposits from six or more earlier events at Driftwood Bay and Stardust Bay. Careful dating procedures establish that some of the coherent deposits in the Aleutian Islands located well above the storm and tidal level are associated with large tsunami inundations in the 18th, 15th and 14th centuries, with the 14th century event having corresponding inundations at the Hawai'i sites. By modeling the spatial distribution of the stratigraphic deposits and exploiting the along-strike variation in deposits between islands, first-order slip models were determined by modeling the tsunami observations in the Aleutian Islands and Hawai'i simultaneously (Yamazaki et al., 2024b). Corrections were made for sea level changes over time for the tsunami calculations.

Fitting the observations and non-observations in the near-field and far-field indicates that the 18th century event ruptured down-dip of the 1957 slip zone on a 100 km wide segment along Umnak Island (Fig. 20) with 26 m slip, the same amount that the shallower segment slipped in 1957. This deeper slip produced sedimentary deposits at elevations of 23 m on Driftwood Bay and 14 m in Stardust Bay, but no deposits in Hawai'i, unlike for the 1957 event. The estimated M_W is 8.4. The 15th century event produced 23 m elevation deposits at Driftwood Bay but was not

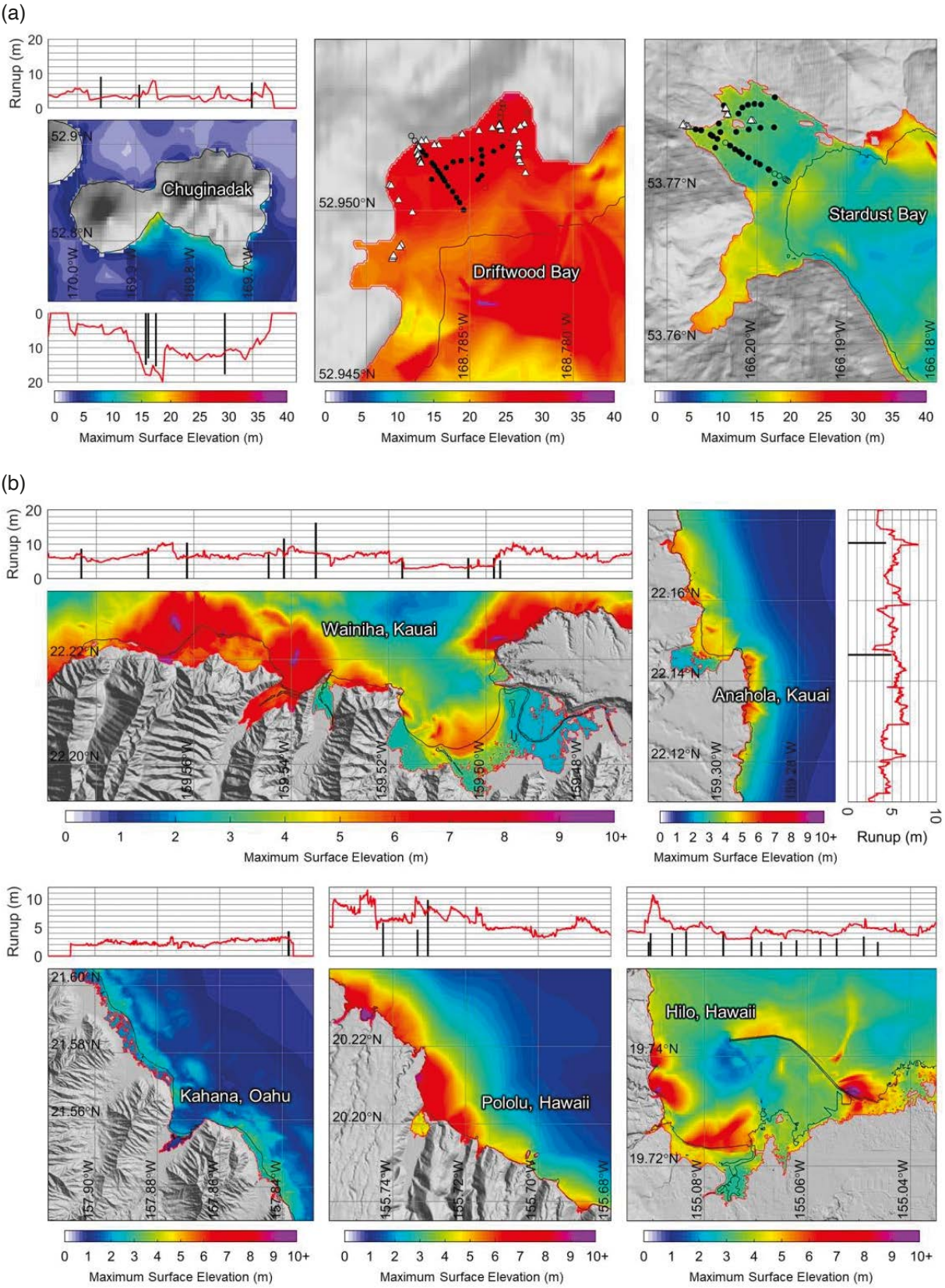

Figure 21. Inundation and runup observations and predictions for the preferred model for the 1957 M_W 8.6-8.8 earthquake model (Fig. 20) of Yamazaki et al. (2024a). (a) Aleutian sites. (b) Hawai'i sites. White triangles indicate observed drift log locations; solid and open black circles denote cores with and without deposits. Black bars denote observed maximum deposit elevations on Chuginadak Island from Griswold et al. (2019) and observed runup heights at Hawai'i sites from Walker (2004). Black lines denote waterlines at local MSL and red lines delineate computed runup heights and inundation limits.

evident at Stardust Bay or in Hawai'i. The data are well modeled with 32 m slip in the shallow segment seaward of Umnak (Fig. 20), giving M_W 7.92, overlying the 26 m slip zone in 1957. This appears to be the first documented repeat of tsunami earthquake failure of shallow megathrust for a Pacific subduction zone (coral records indicate a prior (~1314 A.D.) tsunami earthquake rupture of the 2010 Mentawai, Sumatra tsunami event, Philibosian et al., 2012). If strongly locked, this region could have reaccumulated 32 m of slip deficit by 1957, so the large slip estimate is tectonically viable. The 14th century event produced sedimentary deposits at all of the Aleutian and Hawai'i sites, but with less runup than the 1957 event. Again, balancing the near-field and far-field signals leads to a model with 600 km long rupture with from 7 to 14 m slip down-dip from the 1957 slip zone (Fig. 20). The estimated M_W is 8.6.

For these pre-historic events, the tsunami deposit information is the only basis for quantifying the slip position and strength, and in these cases, even the existence of the earthquakes. The result is a first-order estimate of the slip in great Eastern Aleutian Island earthquakes extending over 7 centuries. This reaffirms the primary tsunami hazard for Hawai'i associated with plate boundary events in this region.

3. Discussion

This review highlights recent applications of tsunami observations in improving spatial constraints on finite-fault slip distributions estimated for large submarine earthquakes. This summary builds on similar prior overviews by Lorito et al. (2016) and Romano et al. (2020a) for important events since 2004, with some new insights emerging. For megathrust earthquakes (Section 2.1 and 2.2), such as the 2021 Chignik, 2020 Simeonof, 2021 Kermadec, 2021 Loyalty, 2022 Sumatra, and to some extent the 2021 South Sandwich Islands events, incorporation of tsunami observations in the estimation of megathrust slip distributions provided valuable constraints on the up-dip extent of slip toward the trench. This is a valuable complement to seismic and geodetic observations, which generally constrain well the down-dip and along-strike distributions of slip. Whether coseismic slip in large ruptures that nucleate down-dip reached the shallow megathrust is directly relevant to the potential for subsequent up-dip rupture in a tsunami earthquake like the 2022 Sumatra event. Of course, very low slip could fail to be detected, but the sensitivity of the first pulse arrival time and amplitude of the seaward tsunami observations is quite striking, especially in the case of rupture under a continental shelf, where there is rapid increase in short period tsunami excitation if deformation reaches beyond the shelf break.

With the widespread interest in shallow megathrust slip deficit and tsunami earthquake potential (e.g., Lay et al., 2012; Cheung et al., 2022), there is strong motivation to incorporate tsunami modeling into rapidly determined rupture models like those produced by the United States Geological Survey National Earthquake Information Center (USGS-NEIC). Efforts to do this are reportedly underway. Tsunami analysis can be combined with teleseismic P coda analysis (e.g., Lay et al., 2019) to rapidly detect slip under deep water near the trench for shallow megathrust event, to alert tsunami warning systems for possibly stronger than normal tsunami amplitudes. Joint inversion of tsunami data with seismic and geodetic observations is often viable, as long as nonlinear behavior is not an issue (e.g., Li et al., 2016a), but this may constrain the tsunami signal that can be used reliably (it is important to upweight the fitting of the first arrival time and amplitude, which limits the signal length). Forward modeling of complete tsunami observations can be done quickly (e.g., Li et al., 2016b; Bai et al., 2022; Liu et al., 2023a), and often provides intuitive guidance on model adjustments, if needed, so it often converges quickly. Tsunami modeling can also evaluate claims of shallow slip occurrence that result from underestimating limitations of seismic and geodetic inversions (e.g., Romano et al., 2021; Lay et al., 2016; Romano et al., 2020b).

An important aspect of the foregoing attributes of including tsunami data in source analyses is that more than just the up-dip limit of slip is constrained. When data with complementary sensitivity to slip distribution are combined, the constraints from each data type influence the overall placement of slip in both joint inversions and iterative modeling. This is evident in the models in Fig. 4 and 9; the down-dip slip distribution is modified significantly when slip is not allowed to be placed in regions where it is precluded by the tsunami data. This is a strong motivation for including complementary data sets such as onshore geodetic and seismic data with tsunami data, as demonstrated in Fig. 1. Too often, researchers decide to simply omit one data set or another because it may, in isolation, have intrinsically low sensitivity to absolute placement of slip on a fault (this is usually the case for teleseismic data on their own), but if independent data tightly constrain the absolute placement of slip, then each data set is essentially stabilized (the solution will no longer project into the null space for the individual inversions), and can contribute to the overall solution.

Other attributes of tsunami data for finite-fault source models include the depth resolution it adds for intraplate faulting like the 2023 Loyalty Islands event, and the constraint on very complex faulting like the 2018 Gulf of Alaska and 2020 Sand Point events (Section 2.3). For the latter event, the tsunami data alone revealed the presence of a significant slow slip component to the source that was not detected by seismic and geodetic data. Tsunami data, complemented by seismic and/or geodetic data helped to resolve the magnitude and depth extent of décollement failure in the 2018 Hawai'i event and the compound-faulting 1975 Kalapana earthquake (Section 2.4).

Joint analysis of near-field and far-field tsunami runup and inundation observations, along with tide gauge data when available, enabled first-order slip models for great earthquakes along the Aleutian Islands to be improved or generated for the first time (Section 2.6). The strategy of simultaneous modeling of all the tsunami observations with non-hydrostatic modeling capabilities that account for differences in wave interactions toward land and dispersion toward sea is clearly demonstrated by these applications, and the update in slip model for the 1957 event is rather remarkable (it was well-anticipated by the prior field studies and preliminary modeling efforts, but a unified model is now available). While tsunami runup and inundation modeling for prehistoric events has long been practiced, there is particular value in simultaneous consideration of near-source and distant observations to improve faulting resolution along dip, as demonstrated in the recent studies.

4. Conclusions

The expanded deployment of seafloor pressure sensors with telemetry since the 2004 Sumatra-Andaman event has greatly impacted earthquake slip model determination for almost all subsequent large shallow submarine earthquake ruptures around the planet. While tsunami waves are very long period, they travel relatively slowly, and the propagation medium is sufficiently well known that robust waveform modeling is often possible. Multiple attributes of tsunami observations are demonstrated by this overview of recent studies of large megathrust events, large intraplate events, and historic earthquakes for which tsunami observations are the primary data. Seaward propagating tsunami data provide valuable constraints on the otherwise poorly resolved up-dip limit of slip for megathrust events. They also can contribute to complex faulting in intraplate events, including detection of slow faulting components that are undetected by seismic and geodetic data. Tsunami data are of great value for locating and estimating slip for older events that predate the era of GNSS and InSAR observations and are not well recorded by seismic data, and tsunami stratigraphic deposits present unique constraints on prehistoric events.

Data availability statement. All data displayed in this review can be accessed through the cited publications. No new data were utilized in this study.

Acknowledgements. T. Lay was supported by the National Science Foundation under gran number EAR-1802364.

References

Abbate, A., J. M. G. Vida, M. J. Castro Diaz, F. Romano et al. (2024). Modeling tsunami initial conditions due to rapid coseismic seafloor displacement: efficient numerical integration and a tool to build unit source databases, Nat. Haz. Earth Sys. Sci., doi:10.5194/nhess-2024-41.

Abrahams, L. S., L. Krenz, E. M. Dunham, A. A. Gabriel et al. (2023). Comparison of methods for coupled earthquake and tsunami modelling, Geophys. J. Inter., 234, 404-426, doi:10.1093/gji/ggad053.

Amezawa, Y., Y. Hiramatsu, A. Miyakawa, K. Imanishi et al. (2023). Long-living earthquake swarm and intermittent seismicity in the northeastern tip of the Noto Peninsula, Japan, Geophys. Res. Lett., 50, e2022GL102670, doi:10.1029/2022GL102670.

Ammon, C. J., H. Kanamori, T. Lay and A. A. Velasco (2006). The 17 July 2006 Java tsunami earthquake, Geophys. Res. Lett., 33, L24308, doi:10.1029/2006GL028005.

Anderson, K. R., I. A. Johanson, M. R. Patrick, M. Gu. et al. (2019). Magma reservoir failure and the onset of caldera collapse at Kilauea Volcano in 2018, Science, 366, eaaz1822, doi:10.1126/science.aaz1822.

Ando, M. (1979). The Hawaii earthquake of November 29, 1975: Low dip angle faulting due to forceful injection of magma, J. Geophys. Res., 84, 7616-7626, doi:10.1029/jb084ib13p07616.

Bai, Y., L. Ye, Y. Yamazaki, T. Lay et al. (2018). The 4 May 2018 M_W 6.9 Hawaii Island earthquake and implications for tsunami hazards, Geophys. Res. Lett., 45, 11040-11049, doi:10.1029/2018GL079742.

Bai, Y., C. Liu, T. Lay, K. F. Cheung et al. (2022). Optimizing a model of coseismic rupture for the 22 July 2020 M_W 7.8 Simeonof earthquake by exploiting acute sensitivity of tsunami excitation across the shelf break, J. Geophys. Res. Solid Earth, 127, e2022JB024484. doi:10.1029/2022JB024484.

Bai, Y., C. Liu, T. Lay, K. F. Cheung et al. (2023). Fast and slow intraplate ruptures during the 19 October 2020 magnitude 7.6 Shumagin earthquake, Nat. Comm., 14, 2015, doi:10.1038/s41467-023-37731-2.

Bilek, S. and T. Lay (1999). Rigidity variations with depth along interplate megathrust faults in subduction zones, Nature, 400, 6743, 443-446, doi:10.1038/22739.

Bilek, S. and T. Lay (2002). Tsunami earthquakes possibly widespread manifestations of frictional conditional stability, Geophys. Res. Lett., 29, 1673, doi:10.1029/2002GL015215.

Boyd, T. M. and J. L. Nabelek (1988). Rupture process of the Andreanof Islands earthquake of May 7, 1986, Bull. Seismol. Soc. Am., 78, 1653-1673.

Brooks, Z. A., D. Goldberg, J. De Santo, T. L. Ericksen et al. (2023). Rapid shallow megathrust afterslip from the 2021 M8.2 Chignik, Alaska earthquake revealed by seafloor geodesy, Sci. Adv., 9, eadf9299, doi:10.1126/sciadv.adf9299.

Byrne, D. E., D. M. Davis and L. R. Sykes (1988). Loci and maximum size of thrust earthquakes and the mechanics of the shallow reigon of subduction zones, Tectonics, 7, 833-857.

Chen, K., J. D. Smith, J. P. Avouac, Z. Liu et al. (2019). Triggering of the M_W 7.2 Hawaii earthquake of 4 May 2018 by a dike intrusion, Geophys. Res. Lett., 46, 2503-2510, doi:10.1029/2018GL081428.

Cheung, K. F., T. Lay, L. Sun and Y. Yamazaki (2022). Tsunami size variability with rupture depth, Nat. Geo., 15, 33-36, doi:10.1038/241561-021-00869.

Chousianitis, K. and A. O. Konca (2021). Rupture process of the 2020 M_W 7.0 Samos earthquake and its effect on surrounding active faults, Geophys. Res. Lett., 48, e2021GL094162, doi:10.1029/2021GL094162.

Crowell, B. W. and D. Melgar (2020). Slipping the Shumagin gap: A kinematic coseismic and early afterslip model of the M_W 7.8 Simeonof Island, Alaska, earthquake, Geophys. Res. Lett., 47, e2020GL090308, doi:10.1029/2020GL090308.

Day, S. J., P. Watts, S. T. Grilli and J. T. Kirby (2005). Mechanical models of the 1975 Kalapana, Hawaii earthquake and tsunami, Mar. Geol., 215, 59-92, doi:10.1016/j.margeo.2004.11.008.

DeMets, C., R. G. Gordon and D. F. Argus (2010). Geologically current plate motions, Geophys. J. Int., 181, 1-80, doi:10.1111/j.1365-246X.2009.04491.x.

DeSanto, J. B., S. C. Webb, S. L. Nooner, D. A. Schmidt et al. (2023). Limited shallow slip for the 2020 Simeonof earthquake, Alaska, constrained by GNSS-Acoustic, Geophys. Res. Lett., 50, e2023GL105045, doi:10.1029/2023GL105045.

Dogan, G. G., A. C. Yalciner, Y. Yuksel, E. Ulutas et al. (2021). The 30 October 2020 Aegean Sea tsunami: Post-event field survey along Turkish coast, Pure Appl. Geophys., 178, 785-812, doi:10.1007/s00024-021-02693-3.

Drooff, C. and J. T. Freymueller (2021). New constraints on slip deficit on the Aleutian megathrust and inflation at Mt. Veniaminof, Alaska from repeat GPS measurements, Geophys. Res. Lett., 48, 4, e2020GL091787, doi:10.1029/2020GL091787.

Eissler, H. K. and H. Kanamori (1987). A single-force model for the 1975 Kalapana, Hawaii earthquake, J. Geophys. Res., 92, 4827-4836, doi:10.1029/jb092ib06p04827.

Elliott, J. L., R. Grapenthin, R. M. Parmeswaran, Z. Xiao et al. (2022). Cascading rupture of a megathrust, Sci. Adv., 8, 18, eabm4131, doi:10.1126/sciadv.abm4131.

Freymueller, J. T., E. N. Suleimani and D. J. Nicolsky (2021). Constraints on the slip distribution of the 1938 M_W 8.3 Alaska Peninsula earthquake from tsunami modeling, Geophys. Res. Lett., 48, 32021GL092812, doi:10.1029/2021GL092812.

Furumoto, A. S. and R. L. Kovach (1979). The Kalapana earthquake of November 29, 1975: An intra-plate earthquake and its relation to geothermal processes, Phys. Earth Planet. Inter., 18, 197-208, doi:10.1016/0031-9201(79)90114-6.

Gabriel, A. A., T. Ulrich, M. Marchandon, J. Biemiller et al. (2023). 3D dynamic rupture modeling of the 6 February 2023, Kahramanmaras, Turkey M_W 7.8 and 7.7 earthquake doublet using early observations, The Seismic Record, 3, 342-356, doi:10.1785/0320230028.

Ganas, A., P. Elias, P. Briole, S. Valkaniotis et al. (2021). Co-seismic and post-seismic deformation, field observations and fault model of the 30 October 2020 M_W = 7.0 Samos earthquake, Aegean Sea, Acta Geophys., 69, 999-1024, doi:10.1007/s11600-021-00599-1.

Goldberg, D. E., P. Koch, D. Melgar, S. Riquelme et al. (2022). Beyond the teleseismic: Introducing regional seismic and geodetic data into routine USGS finite-fault modeling, Seismol. Res. Lett., 93, 3308-3323, doi:10.1785/0220220047.

Griswold, F. R., B. T. MacInnes and B. Higman (2019). Tsunami-based evidence for large eastern Aleutian slip during the 1957 earthquake, Quat. Res., 91, 1045-1058, doi:10.1017/qua.2018.39.

Gusman, A. R., J. Roger, W. Power, B. Fry et al. (2022). The 2021 Loyalty Islands earthquake (M_W 7.7): Tsunami waveform inversion and implications for tsunami forecasting for New Zealand, Earth Space Sci., 9, e2022EA002346, doi:10.1029/2022EA002346.

Hayes, G. P., G. L. Moore, D. E. Portner, M. Hearne et al. (2018). Slab2, a comprehensive subduction zone geometry model, Science, 3652, 58-61, doi:10.1126/science.aat4723.

Heidarzadeh, M. and A. R. Gusman (2021). Source modeling and spectral analysis of the Crete tsunami of 2nd May 2020 along the Hellenic Subduction Zone, offshore Greece, Earth Planets Space, 73, 74, doi:10.1186/s40623-021-01394-4.

Heidarzadeh, M., I. R. Pranantyo, R. Okuwaki, G. G. Dogan et al. (2021). Long tsunami oscillations following the 30 October 2020 M_W 7.0 Aegean Sea earthquake: Observations and modeling, Pure Appl. Geophys., 178, 1531-1548, doi:10.1007/s00024-021-02761-8.

Heidarzadeh, M., A. R. Gusman and I. E. Mulia (2023). The landslide source of the eastern Mediterranean tsunami on 6 February 2023 following the M_W 7.8 Kahramanmaras (Türkiye) inland earthquake, Geosci. Lett., 10, 50, doi:10.1186/s40562-023-00304-8.

Herman, M. W. and K. P. Furlong (2021). Triggering an unexpected earthquake in an uncoupled subduction zone, Sci. Adv., 7, eabf7590, doi:10.1126/sciadv.abf7590.

Herman, M. W., K. P. Furlong and R. Govers (2018). The accumulation of slip deficit in subduction zones in the absence of mechanical coupling: implications for the behavior of megathrust earthquakes, J. Geophys Res. Solid Earth, 123, 8260-8278, doi:10.1029/2018JB016336.

Hill, E. M., H. Yue, S. Barbot, T. Lay et al. (2015). The 2012 M_W 8.6 Wharton basin sequence: A cascade of great earthquakes generated by near-orthogonal, young oceanic mantle faults, J. Geophys. Res. 120, 3723-3747, doi:10.1002/2014JB011703.

Hossen, M. J., A. F. Sheehan and K. Satake (2020). A multi-fault model estimation from tsunami data: An application to the 2018 M7.9 Kodiak earthquake, Pure Appl. Geophys., 177, 1335-1346, doi:10.1007/s00024-020-02433-z.

Hu, G., W. Feng, Y. Wang, L. Li et al. (2022). Source characteristics and exacerbated tsunami hazard of the 2020 M_W 6.9 Samos earthquake in eastern Aegean Sea, J. Geophys. Res. Solid Earth, 127, e2022JB023961, doi:10.1029/2022JB023961.

Hu, G., K. Satake, L. Li and P. Du (2023). Origins of the tsunami following the 2023 Turkey-Syria earthquake, Geophys. Res. Lett., 50, e2023GL103997, doi:10.1029/2023GL1039997.

Iinuma, T., R. Hino, M. Kido, D. Inazu et al. (2012). Coseismic slip distribution of the 2011 off the Pacific coast of Tohoku Earthquake refined by means of seafloor geodetic data, J. Geophys. Res. Solid Earth, 117, B7, doi:10.1029/2012JB009186.

Jia, Z., Z. Zhan and H. Kanamori (2022). The 2021 south Sandwich Island M_W 8.2 earthquake: A slow event sandwiched between regular ruptures, Geophys. Res. Lett., 49, e2021GL097104, doi:10.1029/2021GL097104.

Jiang, Y., P. J. González and R. Bürgmann (2021). Subduction earthquakes controlled by incoming plate geometry: The 2020 M > 7.5 Shumagin, Alaska, earthquake doublet, Earth Planet. Sci. Lett., 584, 117447.

Jolivet, L., C. Faccenna, B. Huet, L. Labrousse et al. (2013). Aegean tectonics: Strain localization, slab tearing and trench retreat, Tectonophysics., 597-598,1-33, doi:10.1016/j.tecto.2012.06.011.

Johnson, J. M., Y. Tanioka, L. J. Ruff, K. Satake et al. (1994). The 1957 great Aleutian earthquake, Pure Appl. Geophys., 142, 3-28.

Kanamori, H. (1972). Mechanism of tsunami earthquakes, Phys. Earth Planet. Inter., 6, 346-359, doi:10.1016/0031-9201(72)90058-1.

Kanamori, H. and M. Kikuchi (1993). The 1992 Nicaragua earthquake: A slow tsunami earthquake associated with subducted sediments, Nature, 361, 6414, 714-716, doi:10.1038/361714a0.

Kato, A. (2024). Implications of fault-valve behavior from immediate aftershocks following the 2023 Mj6.5 earthquake beneath the Noto Peninsula, central Japan, Geophys. Res. Lett., 51, e2023GL106444, doi:10.1029/2023GL106444.

Kehoe, H. L, E. D. Kiser and P. G. Okubo (2019). The rupture process of the 2018 M_W 6.9 Hawaii earthquake as imaged by a genetic algorithm-based back-projection technique, Geophys. Res. Lett., 46, 2467-2474, doi:10.1029/2018GL080397.

Kiratzi, A., C. Papzachos, A. Özacar, A. Pinar et al. (2022). Characteristics of the 2020 Samos earthquake (Aegean Sea) using seismic data, Bull. Earthq. Eng., 20, 7713-7735, doi:10.1007/s10518-021-01239-1.

Krabbenhoeft, A., R. von Huene, J. J. Miller, D. Lange et al. (2018). Strike-slip 23 January 2018 M_W 7.9 Gulf of Alaska rare intraplate earthquake: Complex rupture of a fracture zone system, Sci. Rep., 8, 13706, doi:10.1038/s41598-018-32071-4.

Kuehn, H. (2019). Along-trench Segmentation and Down-dip Limit of the Seismogenic zone at the Eastern Alaska-Aleutian Subduction Zone, Ph.D. Thesis, Dalhousie University, 1-334.

La Selle, S., B. M. Richmond, B. E. Jaffe, A. R. Nelson et al. (2020). Sedimentary evidence of prehistoric distant-source tsunamis in the Hawaiian Islands, Sedimentology, 67, 1249-1273, doi:10.1111/sed.12623.

Lay, T. (2015). The surge of great earthquakes from 2004 to 2014, Earth Planet. Sci. Lett., Frontiers paper, 409, 133-146, doi:10.1016/j.epsl.2014.10.047.

Lay, T. (2018). A review of the rupture characteristics of the 2011 Tohoku-oki M_W 9.1 earthquake, Tectonophysics, 733, 4-36, doi:10.1016/j.tecto.2017.09.022.

Lay, T., H. Kanamori, C. J. Ammon, M. Nettles et al. (2005). The great Sumatra-Andaman earthquake of 26 December 2004, Science, 308, 1127-1133.

Lay, T., L. Li, and K. F. Cheung (2016). Modeling tsunami observations to evaluate a proposed late tsunami earthquake stage for the 16 September 2015 Illapel, Chile, M_W 8.3 earthquake, Geophys. Res. Lett., 43, 7902-7912, doi:10.1002/2016GL070002.

Lay, T., H. Kanamori, C. J. Ammon, K. D. Koper et al. (2012). Depth-varying rupture properties of subduction zone megathrust faults, J. Geophys. Res., 117, B04311, doi:10.1029/2011JB009133.

Lay, T., L. Ye, H. Kanamori and K. Satake (2018a). Constraining the dip of shallow, shallowly dipping thrust events using long-period Love Wave radiation patterns: Applications to the 25 October 2010 Mentawai, Indonesia, and 4 May 2018 Hawaii Island earthquakes, Geophys. Res. Lett., 45, 10,342-10, 349, doi:10.1029/2018GL080042.

Lay, T., L. Ye, Y. Bai, K. F. Cheung et al. (2018b). The 2018 M_W 7.9 Gulf of Alaska earthquake: Multiple fault rupture in the Pacific plate, Geophys. Res. Lett., 45, 9542-9551, doi:10.1029/2018GL079813.

Lay, T., C. Liu and H. Kanamori (2019). Enhancing tsunami warning using P wave coda, J. Geophys. Res. Solid Earth, 124, 10,583-10,609, doi:10.1029/2019JB018221.

Li, L., K. F. Cheung, H. Yue, T. Lay et al. (2016a). Effects of dispersion in tsunami Green's functions and implications for joint inversion with seismic and geodetic data: A case study of the 2010 Mentawai M_W 7.8 earthquake, Geophys. Res. Lett., 43, 11,182-11,191, doi:10.1002/2016GL070970.

Li, L., T. Lay, K. F. Cheung and L. Ye (2016b). Joint modeling of teleseismic and tsunami wave observations to constrain the 16 September 2015 Illapel, Chile, M_W 8.3 earthquake rupture process, Geophys. Res. Lett., 43, 4303-4312, doi:10.1002/2016GL068674.

Li, S. and J. T. Freymueller (2018). Spatial variation of slip behavior beneath the Alaska Peninsula along Alaska-Aleutian subduction zone, Geophys. Res. Lett., 45, 3453-3460, doi:10.1002/2017GL076761.

Lindsey, E. O., R. Mallick, J. A. Hubbard, K. E. Bradley et al. (2021). Slip rate deficit and earthquake potential on shallow megathrusts, Nat. Geosci., 14, 321-326, doi:10.1038/s41561-021-00736-x.

Lipman, P. W., J. P. Lockwood, R. T. Okamura, D. A. Swanson et al. (1985). Ground deformation associated with the 1975 magnitude-7.2 earthquake and resulting changes in activity of Kilauea volcano, Hawaii, U.S. Geological Survey Professional Paper, 1276, 1-45.

Liu, C., T. Lay and X. Xiong (2018). Rupture in the 4 May 2018 M_W 6.9 earthquake seaward of the Kilauea East Rift Zone fissure eruption in Hawaii, Geophys. Res. Lett., 45, 9508-9515, doi:10.1029/2018GL079349.

Liu, C., T. Lay, X. Xiong and Y. Wen (2020). Rupture of the 2020 M_W 7.8 earthquake in the Shumagin Gap inferred from seismic and geodetic observations, Geophys. Res. Lett., 47, 32020GL090806, doi:10.1029/2020GL090806.

Liu, C., T. Lay and X. Xiong (2022). The 29 July 2021 M_W 8.2 Chignik, Alaska Peninsula earthquake rupture inferred from seismic and geodetic observations: Re-rupture of the western 2/3 of the 1938 rupture zone, Geophys. Res. Lett., 49, e2021gl096004, doi:10.1029/2021GL096004.

Liu, C., Y. Bai, T. Lay, Y. Feng et al. (2023a). Megathrust complexity and up-dip extent of slip during the 2021 Chignik, Alaska Peninsula earthquake, Tectonophysics, 854, 229808, doi:10.1016/j.tecto.2023.229808.

Liu, C., T. Lay, R. Wang, T. Taymaz et al. (2023b). Complex multi-fault rupture and triggering during the 2023 earthquake doublet in southeastern Türkiye, Nat. Comm., 14, 55564, doi:10.1038/241467-023-41404-5.

Liu, C., Y. Bai, T. Lay, P. He et al. (2024). Shallow crustal rupture in a major M_W 7.5 earthquake above a deep crustal seismic swarm along the Noto Peninsula in Western Japan, Earth Planet. Sci. Lett., in review.

López, A. M. and E. A. Okal (2006). A seismological reassessment of the source of the 1946 Aleutian tsunami earthquake, Geophys. J. Int., 164, 835-849.

Lorito, S., F. Romano and T. Lay (2016). Tsunamigenic major and great earthquakes (2004-2013): Source processes inverted from seismic, geodetic and sea-level data, R. A. Meyers (ed.), Encyclopedia of Complexity and Systems Science, doi:10.1007/978-3-642-27737-5_641-1.

Lorito, S., J. Selva, A. Amato, A. Y. Babeyko et al. (2023). The tsunami warning triggered in the Mediterranean Sea by the 2023 February 6 M_W 7.8 Türkiye-Syria earthquake: From the present Decision Matrix (DM) to Probabilistic Tsunami Forecasting (PTF), AGU Fall Meeting Abstract NH51D-0509.

Lotto, G. C., E. M. Dunham, T. N. Jeppson and H. J. Tobin (2017). The effect of compliant prisms on subduction zone earthquakes and tsunamis, Earth Planet. Sci. Lett., 458, 213-222, doi:10.1016/j.epsl.2016.10.050

Lythgoe, K., K. Bradley, H. Zeng and S. Wei (2023). Persistent asperities at the Kermadec subduction zone controlled by changes in forearc structure: 1976 and 2021 doublet earthquake, Earth Planet. Sci. Lett., 624, 118465, doi:10.1016/j.epsl.2023.118465.

Ma, K. F., H. Kanamori and K. Satake (1999). Mechanism of the 1975 Kalapana, Hawaii, earthquake inferred from tsunami data, J. Geophys. Res., 104, 13,153-13,167, doi:10.1029/1999JB900073.

Ma, S. (2023). Wedge plasticity and a minimalist dynamic rupture model for the 2011 M_W 9.1 Tohoku-Oki earthquake and tsunami, Tectonophysics, 869, 230146, doi:10.1016/j.tecto.2023.230146.

Ma, Z., H. Zeng, H. Luo, Z. Liu et al. (2024). Slow rupture in a fluid-rich fault zone initiated the 2024 M_W 7.5 Noto earthquake, Science, doi:10.1126/science.ado5143.

Masuda, H., D. Sugawara, A. C. Cheng, A. Suppasri et al. (2024). Modeling the 2024 Noto Peninsula earthquake tsunami: Implications for tsunami sources in the eastern margin of the Japan Sea, Geosci. Lett., 11, 29, doi:10.1186/s40562-024-00344-8.

Medvedeva, A., D. Vydrin, A. Krylov, A. Shiryborova et al. (2023). The Turkish tsunami of 6 February 2023 in the northeastern Mediterranean, Pure Appl. Geophys., 180, 3177-3193, doi:10.1007/s00024-023-03341-8.

Meng, J., O. Sinoplu, Z. Zhou, B. Tokay et al. (2021). Greece and Turkey shaken by African tectonic retreat, Sci. Rep., 11, 6486, doi:10.1038/s41598- -86063-y.

Metz, M., F. Vera, A. Carrillo Ponce, S. Cesca et al. (2022). Seismic and tsunamigenic characteristics of a multimodal rupture of rapid and slow stages: The example of the complex 12 August 2021 South Sandwich earthquake, J. Geophys. Res. Solid Earth, 127, e2022JB024646, doi:10.1029/2022JB024646.

Mulia, I. E., M. Heidarzadeh and K. Satake (2022a). Effects of depth of fault slip and continental shelf geometry on the generation of anomalously long-period tsunami by the July 2020 M_W 7.8 Shumagin (Alaska) earthquake, Geophys. Res. Lett., 49, e2021GL094937, doi:10.1029/2021GL094937.

Mulia, I. E., A. Gusman, M. Heidarzadeh and K. Satake (2022b). Sensitivity of tsunami data to the up-dip extent of the July 2021 M_W 8.2 Alaska earthquake, Seismol. Res. Lett., 93, 4, 1992-2003, doi:10.1785.0220210359.

Murphy, S., A. Scala, A. Herrero, S. Lorito et al. (2016). Shallow slip amplification and enhanced tsunami hazard unravelled by dynamic simulations of mega-thrust earthquakes, Sci. Rep., 6, 35007, doi:10.1038/srep35007.

Murphy, S., G. Di Toro, F. Romano, A. Scala et al. (2018). Tsunamigenic earthquake simulations using experimentally derived friction laws, Earth Planet. Sci. Lett., 486, 155-165, doi:10.1016/j.epsl.2018.01.011.

Nettles, M. and G. Ekström (2004). Long-period source characteristics of the 1975 Kalapana, Hawaii, earthquake, Bull. Seism. Soc. Amer., 94, 422-429, doi:10.1785/0120030090.

Nicolsky, D. J., J. T. Freymueller, R. C. Witter, E. N. Sleimani et al. (2016). Evidence for shallow megathrust slip across the Unalaska seismic gap during the great 1957 Andreanof Islands earthquake, eastern Aleutian Islands, Alaska, Geophys. Res. Lett., 43, 10,328-10,337, doi:10.1002/2016GL070704.

Owen, S. E. and R. Bürgmann (2006). An increment of volcano collapse: Kinematics of the 1975 Kalpana Hawaii earthquake, J. Volcanol. Geotherm., 150, 163-185, doi:10.1016/j.jvolgeores.2005.07.012.

Philibosian, B., K. Sieh, D. H. Natawidjaja, H. W. Chiang et al. (2012). An ancient shallow slip event on the Mentawai segment of the Sunda megathrust, Sumatra, J. Geophys. Res., 117, B05401, doi:10.1029/2011JB009075.

Plicka, V., F. Gallovic, J. Zahradník, A. Serpetsidaki et al. (2022). The 2020 Samos M_W 7. Earthquake: Source model depicting complexity and rupture directivity, Tectonophysics, 843, 229591, doi:10.1016/j.tecto.2022.229591.

Polet, J. and H. Kanamori (2000). Shallow subduction zone earthquakes and their tsunamigenic potential, Geophys. J. Int., 142, 684-702.

Prada, M., P. Galvez, J. Ampuero, V. Sallares et al. (2021). The influence of depth-varying elastic properties of the upper plate on megathrust earthquake rupture dynamics and tsunamigenesis, J. Geophys. Res. Solid Earth, 126, doi:10.1029/2021jb022328.

Ren, C., H. Yue, B. Cao, Y. Zhu et al. (2022). Rupture process of the 2020 $M_W = 6.9$ Samos, Greece earthquake on a segmented fault system constrained from seismic, geodetic and tsunami observations, Tectonophysics, 839, 229497, doi:10.1016/j.tecto.2022.229497.

Robert, W. H., Y. Yamazaki, K. F. Cheung and T. Lay (2024). Tsunami variability for the Loyalty Islands 2021 megathrust and 2023 outer rise M_W 7.7 earthquakes, J. Geophys. Res., Oceans, in review.

Roger, J., B. Pelletier, A. Gusman, W. Power et al. (2023). Potential tsunami hazard of the southern Vanuatu subduction zone: tectonics, case study of the Matthew Island tsunami of 10 February 2021 and implications in regional hazard assessment, Nat. Hazards Earth Syst. Sci., 23, 393-414, doi:10.5194/nhess-23-393-2023.

Romano, F., A. Piatanesi, S. Lorito and K. Hirata (2010). Slip distribution of the 2003 Tokachi-oki M_W 8.1 earthquake from joint inversion of tsunami waveforms and geodetic data, J. Geophys. Res., 115, B11313, doi:10.1029/2009JB006665.

Romano, F., A. Piatanesi, S. Lorito, N. D'Agostino et al. (2012). Clues from joint inversion of tsunami and geodetic data of the 2011 Tohoku-Oki earthquake, Sci. Rep., 2, 385, doi:10.1038/srep00385.

Romano, F. A., A. Piatanesi, S. Lorito, C. Tolomei et al. (2016). Optimal time alignment of tide-gauge tsunami waveforms in nonlinear inversions: application to the 2015 Illapel (Chile) earthquake, Geophys. Res. Lett., 43, 226-311, doi:10.1002/2016GL071310.

Romano, F., S. Lorito, A. Piatanesi and T. Lay (2020a). Fifteen years of (major to great) tsunamigenic earthquakes, Earth Sys. Env. Sci., doi:10.1016/B978-0-12-409548-9.11767-1.

Romano, F., S. Lorito, T. Lay, A. Piatanesi et al. (2020b). Benchmarking the optimal time alignment of tsunami waveforms in nonlinear joint inversions for the M_W 8.8 2010 Maule (Chile) earthquake, Front. Earth Sci., 8, 585429, doi:10.3389/feart.2020.585429.

Romano, F., A. R. Gusman, W. Power, A. Piatanesi et al. (2021). Tsunami source of the 2021 M_W 8.1 Raoul Island earthquake from DART and tide-gauge data inversion, Geophys. Res. Lett., 48, e2021GL094449, doi:10.1029/2021GL094449.

Ruppert, N. A., C. Rollins, A. Zhang, L. Meng et al. (2018). Complex faulting and triggered rupture during the 2018 M_W 7.9 offshore Kodiak, Alaska, earthquake, Geophys. Res. Lett., 45, 7533-7541, doi:10.1029/2018GL078931.

Sakkas, V. (2021). Ground deformation modelling of the 2020 M_W 6.9 Samos earthquake (Greece) based on InSAR and GNSS data, Remote Sens., 2021, 13, 1665, doi:10.3390/rs13091665.

Sallarés, V. and C. R. Ranero (2019). Upper-plate rigidity determines depth-varying rupture behavior of megathrust earthquakes, Nature, 576, 96-1010.

Sallarés, V., M. Prada, S. Riquelme, A. Meléndez et al. (2021). Large slip, long duration, and moderate shaking of the Nicaragua 1992 tsunami earthquake caused by low near-trench rock rigidity, Sci. Adv., 7, eabg8659, doi:10.1126/sciadv.abg8659.

Scala, A., G. Festa, J. P. Vilotte, S. Lorito et al. (2019). Wave interaction of reverse-fault rupture with free surface: Numerical analysis of the dynamic effects and fault opening induced by symmetry breaking, J. Geophys. Res. Solid Earth, 124, 1743-1758, doi:10.1029/2018JB016512.

Scala, A., S. Lorito, F. Romano, S. Murphy et al. (2020). Effect of shallow slip amplification uncertainty on probabilistic tsunami hazard analysis in subduction zones: use of long-term balanced stochastic slip models, Pure Appl. Geophys., 177, 1497-1520, doi:10.1007/s00024-019-02260-x.

Scala, A., S. Lorito, C. Escalante Sánchez, F. Romano et al. (2024). Assessing the optimal tsunami inundation modelling strategy for large earthquakes in subduction zones, J. Geophys. Res., Oceans, 129, e2024JC020941, doi:10.1029/2024JC020941.

Scholz, C. H. (1998). Earthquakes and friction laws, Nature, 391, 37-42.

Selva, J., S. Lorito, M. Volpe, F. Romano et al. (2021). Probabilistic tsunami forecasting for early warning, Nat. Commun., 12, 5677, doi:10.1038/s41467-021-25815-w.

Shearer, P. M. and R. Bürgmann (2010). Lessons learned from the 2004 Sumatra-Andaman megathrust rupture, Annu. Rev. Earth Planet Sci., 38, 103-131, doi:10.1146/annurev-earth-040809-152537.

Sun, Y. S., D. Melgar, A. Ruiz-Angulo, A. Ganas et al. (2024). The 2020 M_W 7.0 Samos (Eastern Aegean Sea) earthquake: joint source inversion of multitype data, and tsunami modeling, Geophys. J. Int., 237, 1285-1300, doi:10.1093/gji/ggae082.

Syrianto, S. P. D., A. Arimuko, A. Nurokhim, I. Gunawan et al. (2023). Source characteristics of the 18 November 2022 earthquake (M_W 6.7), offshore southwest Sumatra, Indonesia, revealed by tsunami waveform analysis: Implications for tsunami hazard assessment, Pure Appl. Geophys., 180, 3655-3670.

Tanioka, Y. and K. Satake (1996). Tsunami generation by horizontal displacement of ocean bottom, Geophys. Res. Lett., 23, 861-864, doi:10.1029/96GL00736.

Tanioka, Y. and F. I. González (1998). The Aleutian earthquake of June 10, 1996 (M_W 7.9) ruptured parts of both the Andreanof and Delarof segments, Geophys. Res. Lett., 25, 2245-2248.

Taymaz, T., S. Yolsal-Cevikbilen, T. S. Irmak, F. Vera et al. (2022). Kinematics of the 30 October 2020 M_W 7.0 Néon Karlovásion (Samos) earthquake in the Eastern Aegean Sea: Implications on source characteristics and dynamic rupture simulations, Tectonophysics, 826, 229223, doi:10.1016/j.tecto.2022.229223.

Triantafyllou, I., M. Gogou, S. Mavroulis, E. Lekkas et al. (2021). The tsunami caused by the 30 October 2020 Samos (Aegean Sea) M_W 7.0 earthquake: Hydrodynamic features, source properties and impact assessment from post-event field survey and video Records, J. Mar. Sci. Eng., 2021, 9, 68, doi:10.3390/jmse9010068.

Walker, D. (2004). Regional tsunami evacuations for the state of Hawaii: A feasibility study on historical runup data, Sci. Tsunami Hazards, 22, 3-22.

Wan, Z., D. Wang, J. Zhang, Q. Li et al. (2022). Two-staged rupture of the 19 October 2020 M_W 7.6 strike-slip earthquake illuminated the boundary of coupling variation in the Shumagin Islands, Alaska, Seismol. Res. Lett., 94, 52-65, doi:10.1785/0220220203.

Wang, K., R. E. Thomson, A. B. Rabinovich, I. V. Fine et al. (2020). The 2018 Alaska-Kodiak tsunami off the west coast of North America: A rare mid-plate tsunamigenic event, Pure Appl. Geophys., 177, 1347-1378, doi:10.1007/s00024-020-02427-x.

Wang, Y., M. Heidarzadeh, K. Satake and G. Hu (2022). Characteristics of two tsunami generated by successive M_W 7.4 and M_W 8.1 earthquakes in the Kermadec Islands on 4 March 2021, Natural Haz. Earth Sys. Sci., 22, 1073-1082, doi:10.5194/nhess-22-1073-2022.

Watada, S. (2013). Tsunami speed variations in density-stratified compressible global oceans, Geophys. Res. Lett., 40, 4001-4006, doi:10.1002/grl.50785.

Watada, S., S. Kusumoto and K. Satake (2014). Traveltime delay and initial phase reversal of distant tsunamis coupled with the self-gravitating elastic Earth, J. Geophys. Res., 119, 4287-4310, doi:10.1002/2013JB010841.

Wen, Y., Z. Guo, C. Xu, G. Xu et al. (2019). Coseismic and postseismic deformation associated with the 2018 M_W 7.9 Kodiak, Alaska, earthquake from low-rate and high-rate GPS observations, Bull. Seism. Soc. Am., 109, 908-918, doi:10.1785/0120180246.

Williamson, A. L. and A. V. Newman (2018). Limitations of the resolvability of finite-fault models using static land-based geodesy and open-ocean tsunami waveforms, J. Geophys. Res. Solid Earth, 123, 9034-9048, doi:10.1029/2018JB016091.

Witter, R. C., G. A. Carver, R. W. Briggs, G. Gelfenbaum et al. (2016), Unusually large tsunamis frequent a currently creeping part of the Aleutian megathrust, Geophys. Res. Lett., 43, 76-84, doi:10.1002/2015GL066083.

Witter, R., R. Briggs, S. E. Engelhart, G. Gelfenbaum et al. (2019). Evidence for frequent, large tsunami spanning locked and creeping parts of the Aleutian megathrust, Geol. Soc. Am. Bull., 131, 707-729, doi:10.1130/B32031.1.

Xia, T., L. Ye, Y. Bai, T. Lay et al. (2024). The 2022 M_W 7.3 southern Sumatra tsunami earthquake: Rupture up-dip of the 2007 M_W 8.3 Bengkulu event, J. Geophys. Res. Solid Earth, in revision.

Xiao, Z., J. T. Freymueller, R. Grapenthin, J. L. Elliott et al. (2021). The deep Shumagin gap filled: Kinematic rupture model and slip budget analysis of the 2020 M_W 7.8 Simeonof earthquake constrained by GNSS, global seismic waveforms, and floating InSAR, Earth Planet. Sci. Lett., 576, 117241, doi:10.1016/j.epsl.2021.117241.

Yamazaki, Y., K. F. Cheung and T. Lay (2018). A self-consistent fault slip model for the 2011 Tohoku earthquake and tsunami, J. Geophys. Res. Solid Earth, 123, 1435-1458, doi:10.1002/2017JB014749.

Yamazai, Y., T. Lay and K. F. Cheung (2021). A compound faulting model for the 1975 Kalapana, Hawaii, earthquake, landslide and tsunami, J. Geophys. Res. Solid Earth, 126, e2021JB022488, doi:10.1029/2021JB022488.

Yamazaki, Y., Y. Bai, L. L. Goo, K. F. Cheung et al. (2023). Nonhydrostatic modeling of tsunamis from earthquake rupture to coastal impact, J. Hydraul. Eng., 149, 9, ASCE, ISSN:0733-9429, doi:10.1061/JHEND8.HYENG-13388.

Yamazaki, Y., T. Lay, K. F. Cheung, R. C. Witter et al. (2024a). A great tsunami earthquake component of the 1957 Aleutian Islands earthquake, Earth Planet. Sci. Lett., 637, 118691, doi:10.1016/j.epsl.2024.118691.

Yamazaki, Y., K. F. Cheung, T. Lay, S. P. M. La Selle et al. (2024b). A 700-year rupture sequence of great eastern Aleutian earthquake from tsunami deposits, Nat. Comm., in review.

Yanagisawa, H., I. Abe and T. Baba (2024). What was the source of the nonseismic tsunami that occurred in Toyama Bay during the 2024 Noto Peninsula earthquake, Sci. Rep.,14, 18245, doi:10.1038/s41598-024-69097-w.

Ye, L., H. Kanamori, J. P. Avouac, L. Li et al. (2016). The 16 April 2016, M_W 7.8 (MS 7.5) Ecuador earthquake: A quasi-repeat of the 1942 MS 7.5 earthquake and partial re-rupture of the 1906 MS 8.6 Colombia-Ecuador earthquake, Earth Planet. Sci. Lett., 454, 248-258, doi:10.1016/j.epsl.2016.09.006.

Ye, L, W. Gong, T. Lay, H. Kanamori et al. (2021a). Shallow megathrust rupture during the 10 February 2021 M_W 7.7 southeast Loyalty Islands earthquake sequence, The Seismic Record, 1, 3, 154-163, doi:10.1785/0320210035.

Ye, L., T. Lay, H. Kanamori, Y. Yamazaki et al. (2021b). The 22 July 2020 M_W 7.8 Shumagin seismic gap earthquake: Partial rupture of a weakly coupled megathrust, Earth Planet. Sci. Lett., 562, 116879, doi:10.1016/j.epsl.2021.116879.

Ye, L., Y. Bai, D. Si, T. Lay et al. (2022). Rupture model for the 29 July 2021 M_W 8.2 Chignik, Alaska earthquake constrained by seismic, geodetic, and tsunami observations, J. Geophys. Res. Solid Earth, 127, e2021JB023676, doi:10.1029/2021JB023676.

Ye, L., Y. Hu, D. Si, T. Lay et al. (2024) The 2021 M_W 8.1 Kermadec earthquake sequence: Rupture along the slab/mantle contact, J. Geophys. Res. Solid Earth, in review.

Yokota, Y., K. Koketsu, Y. Fujii, K. Satake et al. (2011). Joint inversion of strong motion, teleseismic, geodetic, and tsunami datasets for the rupture process of the 2011 Tohoku earthquake, Geophys. Res. Lett., 38, L00G21, doi:10.1029/2011gL050098.

Yoshida, K., M. Uno, T. Matsuzawa, Y. Yukutake et al. (2023), Upward earthquake swarm migration in the northeastern Noto Peninsula, Japan, initiated from a deep ring-shaped cluster: Possibility of fluid leakage from a hidden magma system, J. Geophys. Res. Solid Earth, 128, e2022JB026047, doi:10.1029/2022JB026047.

Yue, H., T. Lay, L. Rivera, C. An et al. (2014a). Localized fault slip to the trench in the 2010 Maule, Chile MW = 8.8 earthquake from joint inversion of high-rate GPS, teleseismic body waves, InSAR, campaign GPS, and tsunami observations, J. Geophys. Res., 119, doi:10.1002/2014JB011340.

Yue, H., T. Lay, L. Rivera, Y. Bai et al. (2014b). Rupture process of the 2010 M_W 7.8 Mentawai tsunami earthquake from joint inversion of near-field hr-GPS and teleseismic body wave recordings constrained by tsunami observations, J. Geophys. Res. Solid Earth, 119, 5574-5593, doi:10.1002/2014JB011082.

Zhao, B., Y. Qi, D. Wang, J. Yu et al. (2018). Coseismic slip model of the 2018 M_W 7.9 Gulf of Alaska earthquake and its seismic hazard implications, Seismol. Res. Lett., 90, 642-648, doi:10.1785/0220180141.

Zhao, B., R. Bürgmann, D. Wang, J. Zhang et al. (2022). Aseismic slip and recent ruptures of persistent asperities along the Alaska-Aleutian subduction zone, Nat. Comm., 13, 3098, doi:10.1038/s41467-022-30883-7.

Zhou, Y., W. Wang, J. He, X. Wang et al. (2022), The 19 October 2020 M_W 7.6 earthquake in Shumagin, Alaska: An unusual dextral strike-slip event, Pure Appl. Geophys., 179, 3527-3542, doi:10.1007/s00024-022-03001-3.

***CORRESPONDING AUTHOR: Thorne LAY**,
University of California Santa Cruz, Earth and Planetary Sciences, Santa Cruz, CA, USA
e-mail: tlay@ucsc.edu